

# Optimizing Bidentate *N*-Heterocyclic Carbene Ligands for the Modification of Late Transition Metal Surfaces – New Insights Through Theory

## Supplementary Information

Melanie C. Börner and Johannes Neugebauer\*

Theoretische Organische Chemie, Organisch-Chemisches Institut  
and Center for Multiscale Theory and Computation,  
Westfälische Wilhelms-Universität Münster  
Corrensstraße 40, 48149 Münster, Germany

---

\*email: [j.neugebauer@uni-muenster.de](mailto:j.neugebauer@uni-muenster.de)

# Contents

<b>1</b>	<b>Optimization of the Calculation Setup</b>	<b>3</b>
1.1	Choice of the Energy Cutoff . . . . .	4
1.2	Number of $k$ -Points . . . . .	6
1.3	Size of the Vacuum Layer . . . . .	8
1.4	Distance Between Periodic Images of the Adsorbates . . . . .	11
1.5	Choice of the Type of Surface Under Study . . . . .	13
<b>2</b>	<b>Tilt and Rotation of the NHC Units</b>	<b>17</b>
<b>3</b>	<b>Investigated Conformers</b>	<b>19</b>
<b>4</b>	<b>Adsorption Geometries of All Investigated Ligands</b>	<b>25</b>
<b>5</b>	<b>Acknowledgements</b>	<b>38</b>
<b>6</b>	<b>References</b>	<b>38</b>

# 1 Optimization of the Calculation Setup

Prior to all calculations performed in this work, the calculation setup was carefully optimized as described in the following sections. Since periodic DFT calculations are particularly demanding in terms of the required computational resources, a thorough assessment of the cost/performance ratio is of utmost importance in this area of research.

Firstly, two different the exchange–correlation functionals were tested. The PBE-D3<sup>1-7</sup> approach was compared to the optB88-vdW<sup>8,9</sup> functional. For these calculations, the adsorption of IMe on a 5x5x4 Au slab was selected as model system. Geometry optimizations starting from different orientations of the adsorbate on the slab as well as single point calculations with preselected orientations of the NHC on the surface were performed and the resulting geometries and energies were compared. It was found that both functionals converge to the same adsorption geometry, with IMe sitting upright on-top of an Au atom. Moreover, the energetic trends when the NHC is fixed at different degrees of tilt are the same for the PBE-D3 approach and the optB88-VDW exchange-correlation functional. The adsorption energies determined with these two methods are shifted by approximately 10 kJ/mol, where PBE-D3 predicts stronger adsorption. This deviation is reasonably small. Having confirmed that both functionals predict the same adsorption behavior of IMe, the PBE-D3 method was used for all further calculations, because it requires a considerably lower amount of computational resources.

As a second step, several factors related to periodic DFT calculations were investigated: The choice of the energy cutoff of the plane-wave basis set as well as the number of  $\mathbf{k}$ -points used to sample the Brillouin zone and the size of the unit cell affect the accuracy and the cost of the calculations. Moreover, using the same or at least a very similar setup is essential for the comparability of the results. For this reason, the convergence of the adsorption energies with respect to the above-mentioned parameters was confirmed

before the production calculations were performed. For these tests, Cu, Pd, and Au slabs consisting of 8x8x4 metal atoms were used and IMe was chosen as adsorbate.

## 1.1 Choice of the Energy Cutoff

In order to assess the cost/performance ratio of different energy cutoffs, single point (SP) energy calculations were carried out, in which all parameters except for the energy cutoff were kept fixed. All calculations were successively performed on the same 72-core Intel Xeon Gold 6140 machine running at 2.30 GHz, thereby ensuring the comparability of the determined timings. The relaxed structures of IMe on the Cu, Pd and Au slabs as well as the relaxed clean metal surfaces and the relaxed IMe molecule in the corresponding unit cells served as geometries for the computation of the adsorption energies. Energy cutoffs between 200 eV and 700 eV were studied in steps of 50 eV, and the relative adsorption energies as well as the required CPU times were compared. The energy values obtained with the most accurate setup (energy cutoff = 700 eV) were used as references. Fig. S1 summarizes the results. It can be seen that the adsorption energies of IMe on the three different metal surfaces are well converged if energy cutoffs of 350 eV or higher are used: The differences in the relative adsorption energies vary by no more than 1.3 kJ/mol, for Cu(111) and Pd(111) the differences are even smaller than 1.0 kJ/mol. Moreover, especially for Pd(111) and Au(111), the required CPU times for the calculations increase substantially when energy cutoffs above 500 eV are used. We therefore dissuade from using energy cutoffs below 350 eV and above 500 eV.

While the adsorption energies on the different metal surfaces converge relatively fast with respect to the energy cutoff, the deviations observed for the total energies used to calculate these adsorption energies (Eq. 1) are much stronger. This is shown for the adsorption of IMe on the Cu(111) surface in Fig. S2. It can be seen that the relative total energies of the adsorbed system “slab+NHC” and the clean slab “slab” have a very similar convergence

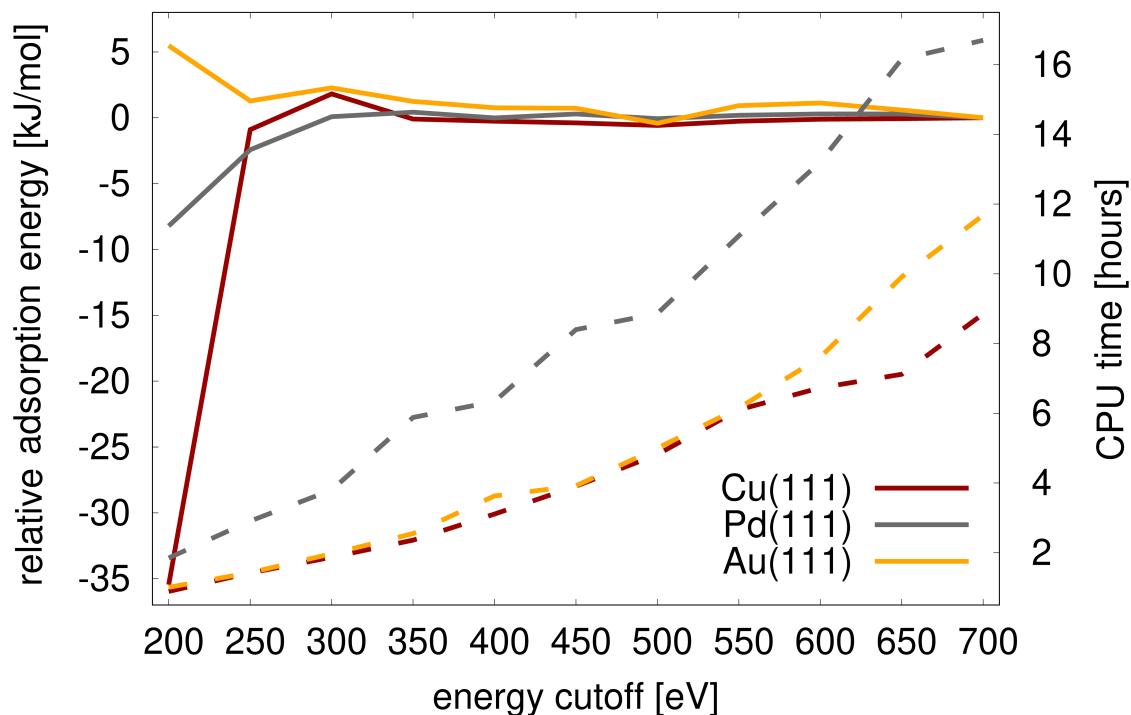


**Figure S1:** Comparison of the relative adsorption energies (solid lines) and the cost (dashed lines) of calculations employing energy cutoffs between 200 eV and 700 eV. The data sets for adsorption on the Cu(111), Pd(111) and Au(111) surfaces are illustrated in red, gray and orange, respectively. The adsorption energy values obtained with the most accurate setup (energy cutoff = 700 eV) were used as references. All calculations were successively performed on the same 72-core Intel Xeon Gold 6140 machine running at 2.30 GHz.

behavior, which explains the comparatively high stability of the adsorption energy with respect to the energy cutoff (see Fig. S1 and Eq. 1). However, an energy cutoff of at least 450 eV is required to achieve convergence of the adsorbed system and clean slab total energies.

In order to reduce the computational effort while ensuring high accuracy of the results, geometry optimizations can be performed stepwise. A less expensive setup (e.g. an energy cutoff of 350 eV or 400 eV) can be used to obtain a reasonable (adsorption) geometry, while a tighter setup is applied to fine-tune the geometry and obtain highly accurate energies. Such a pre-optimization technique was applied in the present work: an energy cutoff of 400 eV was used for pre-optimizations up to a maximum force component of  $0.03 \text{ eV}/\text{\AA}$ .

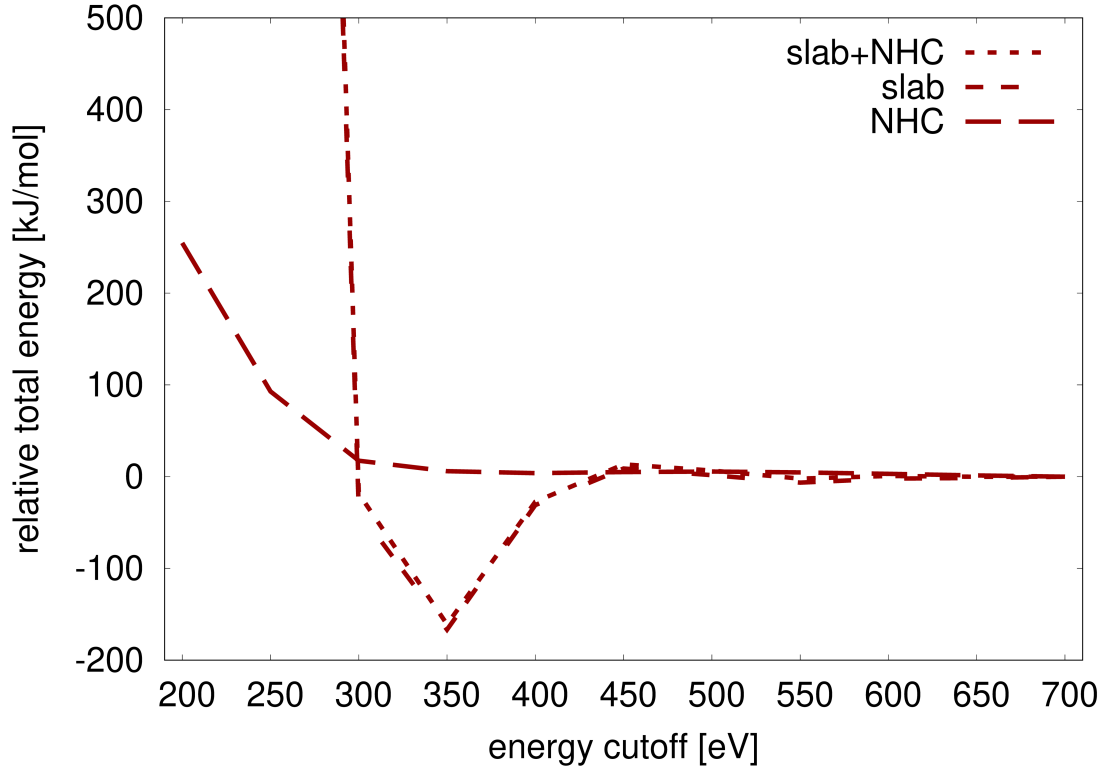


**Figure S2:** Convergence of the relative total energies used to calculate the adsorption energy of IMe on the Cu(111) surface with respect to the energy cutoff. The relative total energies of the adsorbed structure (slab+NHC), the clean Cu(111) slab (slab), and the isolated adsorbate in the respective unit cell (NHC) are plotted against the energy cutoff. The total energy values obtained with the most accurate setup (energy cutoff = 700 eV) were used as references.

During the pre-optimizations, the SCF convergence criterion was loosened to  $10^{-4}$  eV. The pre-converged structures were subsequently re-optimized using tighter conditions: The energy cutoff was increased to 500 eV, the maximum force component was reduced to  $0.01$  eV/Å and the SCF convergence criterion was set to  $10^{-6}$  eV.

## 1.2 Number of $k$ -Points

The cost/performance ratio of an increasing number of  $k$ -points in the surface directions (*i.e.* in the directions of the lattice vectors  $\mathbf{a}_1$  and  $\mathbf{a}_2$ ) was studied in a similar fashion as

the performance of different energy cutoffs. SP calculations on the same test systems (see above) were carried out and all parameters except for the number of  $\mathbf{k}$ -points in the surface directions were kept fixed. In the direction perpendicular to the surface, one  $\mathbf{k}$ -point was utilized. Again, all calculations were successively performed on the same 72-core Intel Xeon Gold 6140 machine running at 2.30 GHz. The relative adsorption energies and the CPU time required for the calculation of the data are compared in Fig. S3. The energy values obtained with the most accurate setup (6x6x1  $\mathbf{k}$ -points) were used as references. It

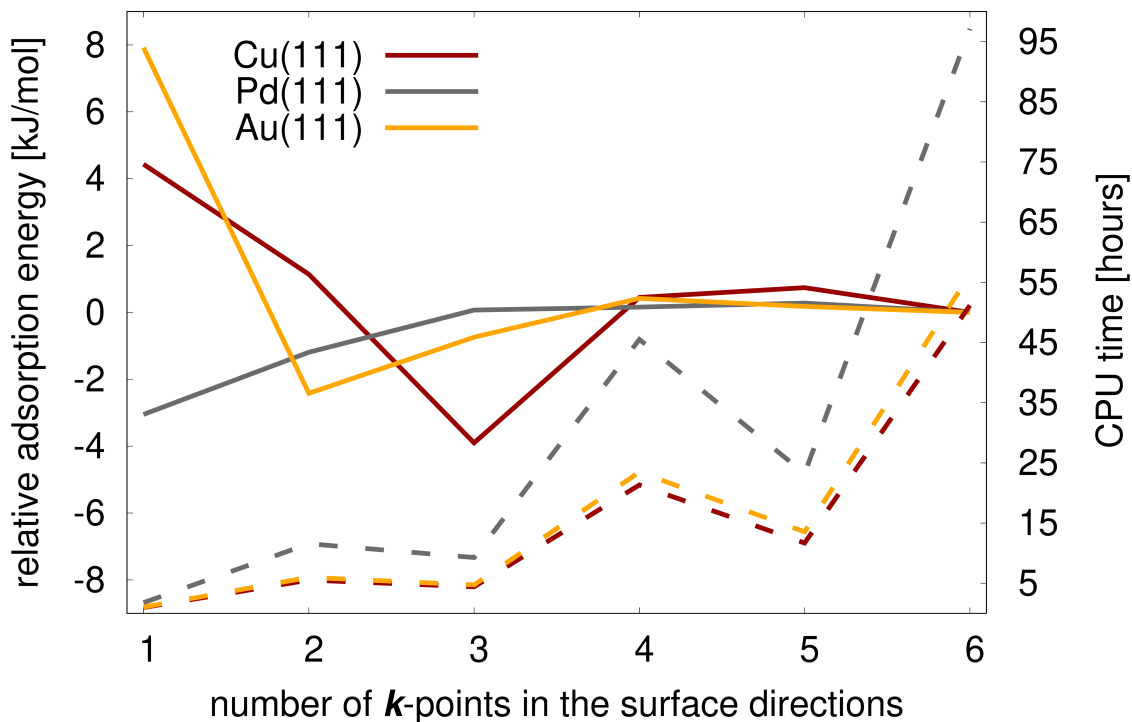


**Figure S3:** Comparison of the relative adsorption energies (solid lines) and the cost (dashed lines) of calculations employing between one and six  $\mathbf{k}$ -points in the surface directions. The data sets for adsorption on the Cu(111), Pd(111) and Au(111) surfaces are illustrated in red, gray and orange, respectively. The adsorption energy values obtained with the most accurate setup (6  $\mathbf{k}$ -points in the surface directions) were used as references. All calculations were successively performed on the same 72-core Intel Xeon Gold 6140 machine running at 2.30 GHz.

can be seen that the adsorption energy on the Pd(111) and Au(111) surfaces changes by less than 1.0 kJ/mol if three or more  $\mathbf{k}$ -points in the surface directions are used to sample the first Brillouin Zone (BZ). This indicates that using 3x3x1  $\mathbf{k}$ -points is sufficient for unit

cells of this size. For Cu(111), the convergence is slightly worse. The relative adsorption energies of IMe computed with 3x3x1 or 6x6x1  $\mathbf{k}$ -points differ by 3.90 kJ/mol, which is still an acceptable deviation. A possible reason for this is the smaller lattice constant of Cu compared to Au and Pd, which results in a smaller unit cell if the metal slabs are equally large. Since larger unit cells in real space correspond to smaller BZs, they require less  $\mathbf{k}$ -points to obtain accurate results.<sup>10</sup> Consequently, the larger Au and Pd unit cells converge faster with the number of  $\mathbf{k}$ -points. In order to improve the convergence for the Cu(111) slab, the number of  $\mathbf{k}$ -points, or the number of atoms (*i.e.* the size of the unit cell) could be increased.

With regard to the timings, it can be observed that odd numbers of  $\mathbf{k}$ -points perform much better than even ones do. This is due to the distribution of  $\mathbf{k}$ -points in the first BZ according to the Monkhorst-Pack<sup>11</sup>  $\mathbf{k}$ -point sampling method.<sup>12</sup> Fig. S3 clearly shows that the increase of the required CPU time with a rising number of  $\mathbf{k}$ -points is immense. Although utilizing four (or five)  $\mathbf{k}$ -points in the surface directions improves the value of the relative adsorption energies on Cu(111), this improvement comes at such a high computational cost that this is hardly an option. We therefore recommend using three  $\mathbf{k}$ -points in the surface directions for unit cells of similar size as those in this work.

### 1.3 Size of the Vacuum Layer

In order to produce reliable results, the vacuum layer that separates two adjacent periodic images of the surface model needs to be large enough to ensure that interactions between the replicas are prohibited. Technically, this means that the height of the unit cell, *i.e.* the lattice vector  $\mathbf{a}_3$ , must be chosen appropriately large (see Fig. S4). In order to determine the necessary height of the unit cell, the convergence of the adsorption energy of IMe on the Cu(111), Pd(111) and Au(111) surfaces with respect to the size of the lattice vector  $\mathbf{a}_3$  was tested. SP calculations on the same systems as for the determination of

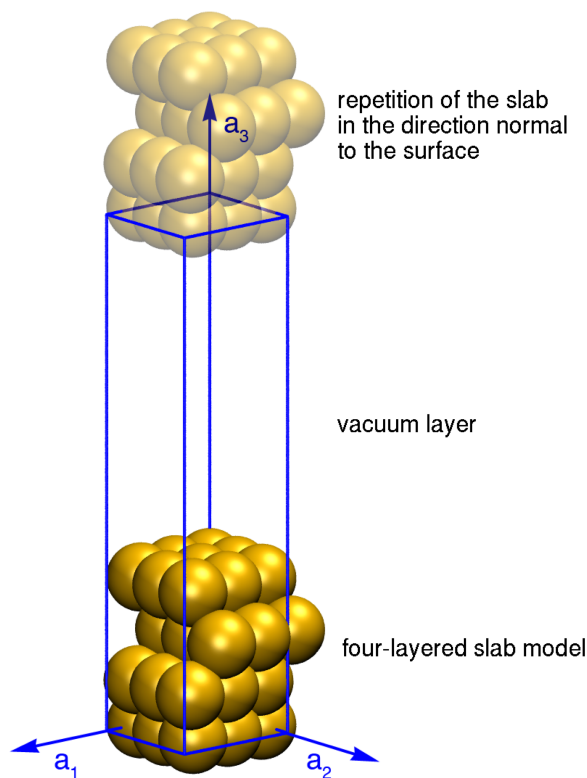


**Figure S4:** Illustration of an asymmetric slab model containing  $3 \times 3$  atoms and four atomic layers. The unit cell is displayed as blue box and the directions of the lattice vectors  $\mathbf{a}_i$  are indicated by blue arrows.

the energy cutoff and the number of  $\mathbf{k}$ -points were performed (see above). The height of the unit cells was varied from  $15.0 \text{ \AA}$  to  $40.0 \text{ \AA}$ . The step width was set to  $1.0 \text{ \AA}$ , and all other parameters were kept fixed. Once more, all calculations were successively performed on the same 72-core Intel Xeon Gold 6140 machine running at 2.30 GHz. The relative adsorption energies and the CPU time required for the calculation of the data are compared in Fig. S5. The energy values obtained with the most accurate setup ( $|\mathbf{a}_3| = 40.0 \text{ \AA}$ ) were used as references. Fig. S5 shows that, for small unit cells ( $|\mathbf{a}_3| < 17.0 \text{ \AA}$ ), the adsorption energy is strongly dependent on the unit cell height. This indicates artificial interactions between adjacent periodic replicas. With increasing height, the dependence decreases. For  $|\mathbf{a}_3| > 17.0 \text{ \AA}$ , the relative adsorption energies vary by less than  $5.0 \text{ kJ/mol}$  on all three metal surfaces. On the Cu(111) and Pd(111) surfaces, unit cell heights of  $21.0 \text{ \AA}$  and  $22.0 \text{ \AA}$  are sufficient to reach independence of the adsorption energy from  $|\mathbf{a}_3|$

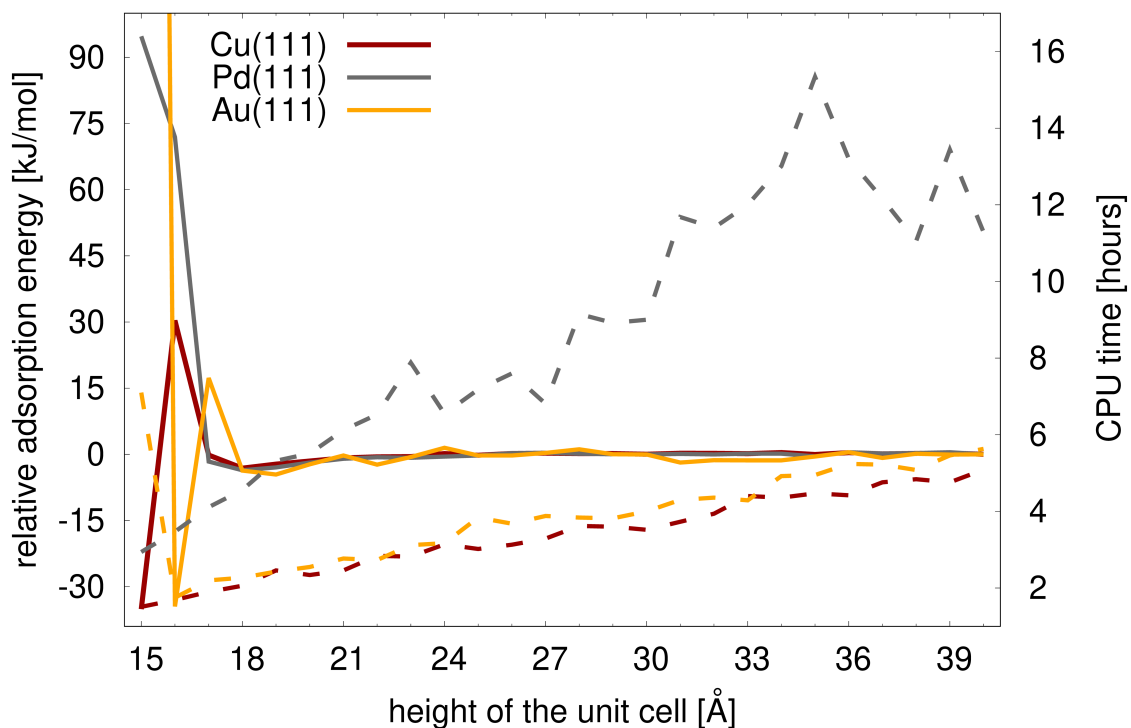


**Figure S5:** Comparison of the relative adsorption energies (solid lines) and the cost (dashed lines) of calculations using different heights of the unit cell. The data sets for adsorption on the Cu(111), Pd(111) and Au(111) surfaces are illustrated in red, gray and orange, respectively. The adsorption energy values obtained with the most accurate setup ( $|\mathbf{a}_3| = 40.0 \text{ \AA}$ ) were used as references. All calculations were successively performed on the same 72-core Intel Xeon Gold 6140 machine running at 2.30 GHz.

(variations  $< 1.0 \text{ kJ/mol}$ ). In order to reach full convergence on the Au(111) surface, however, the unit cells must be as high as  $35.0 \text{ \AA}$ .

With regard to the CPU time (Fig. S5, dashed lines), it can be said that the unit cell height has a moderate influence on the cost of the calculations on the Cu(111) and Au(111) surfaces. However, for the Pd(111) surface, the additional vacuum space comes at a higher cost. When choosing the height of the unit cells, it should also be considered that the unit cell size must be set *before* a geometry is optimized. Considerable structural rearrangements can take place during a geometry optimization and interactions between periodic images must be prohibited at all times. It can therefore be concluded that a unit cell height of around  $22.0 \text{ \AA}$  might suffice for the SP energy calculations presented in this

section, but is too small to allow for unbiased geometry optimizations, especially if large and flexible adsorbates (such as bidentate NHC-ligands) are involved. In order to avoid any interactions between the periodic replicas at all times, a unit cell height of 35.0 Å was applied in all calculations presented in this work.

## 1.4 Distance Between Periodic Images of the Adsorbates

The length and the width of the unit cell are two more factors influencing the accuracy and time requirements of periodic DFT calculations. The size of the surface section included in the unit cell determines the surface coverage, *i.e.* the distance between the periodic images of adsorbates on the surface. In this work, the focus lies on the investigation of independent adsorbates and, consequently, the unit cell must be chosen large enough to ensure that the periodic images do not interact. Note that this approach corresponds to a rather low surface coverage and that adsorbates in self-assembled monolayers are often more closely packed. However, studying independent adsorbates allows for the calculation of accurate adsorption energies, which are important reference data for future investigations on more densely packed systems. The necessary distance between the adsorbates can be determined by very simple test calculations. It is sufficient to relax the structure and calculate the total energy of a single adsorbate molecule in unit cells of increasing size. The unit cell is large enough when the total energy becomes independent from its size.

In this work, IMe was chosen as model adsorbate to determine the minimum distance between adsorbates on the surface. Four adjacent periodic replicas of IMe are shown in Fig. S6 and the smallest distance  $d$  between atoms of neighboring images in the directions of lattice vectors  $\mathbf{a}_1$  and  $\mathbf{a}_2$  is indicated by black arrows. Here, an orthorhombic unit cell was employed and the lattice vectors (in Å) were

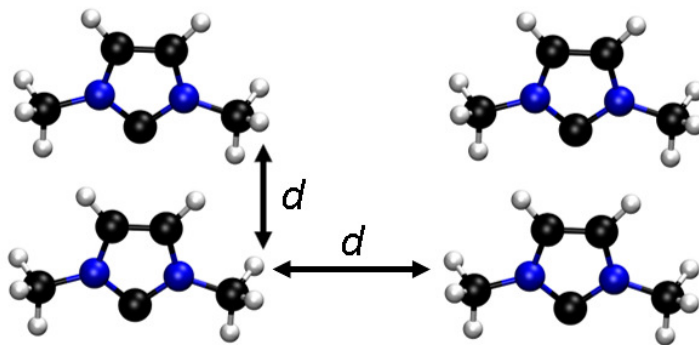


**Figure S6:** Illustration of the minimal distance  $d$  between periodic images of IMe adsorbates. C atoms are illustrated in black, N atoms are blue and H atoms are displayed in white.

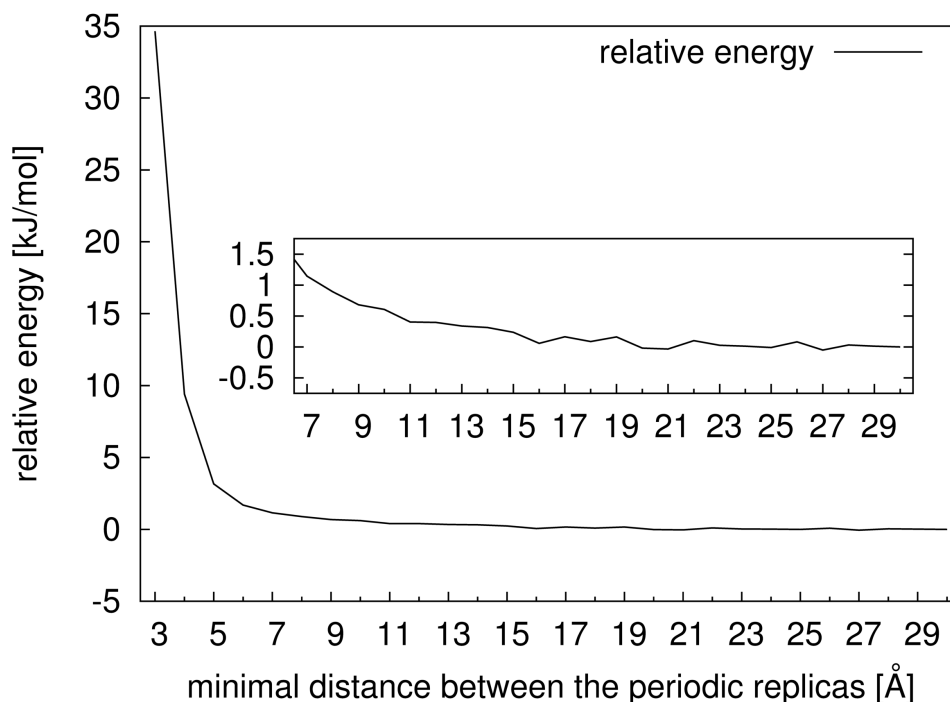


**Figure S7:** Convergence of the relative total energy of an IMe molecule with an increasing size of the unit cell in the directions of the lattice vectors  $\mathbf{a}_1$  and  $\mathbf{a}_2$ . The unit cell size was chosen such that the minimal distance  $d$  between atoms of neighboring periodic replicas of the molecule in the direction of  $\mathbf{a}_1$  and  $\mathbf{a}_2$  was equal. Values for  $d$  between 3.0 Å and 30.0 Å were studied. The converging region of the relative total energy is enlarged. The total energy obtained for the largest unit cell (with  $d = 30.0$  Å) was employed as reference.

$$\mathbf{a}_1 = \begin{pmatrix} 6.00 + d \\ 0.00 \\ 0.00 \end{pmatrix}, \quad \mathbf{a}_2 = \begin{pmatrix} 0.00 \\ 1.85 + d \\ 0.00 \end{pmatrix} \quad \text{and} \quad \mathbf{a}_3 = \begin{pmatrix} 0.00 \\ 0.00 \\ 33.85 \end{pmatrix}, \quad (1)$$

where  $d$  was increased from 3.0 Å to 30.0 Å. The step width was 1.0 Å. Since a single molecule was studied in this set of calculations, only one  $\mathbf{k}$ -point was used in each dimension.

Fig. S7 shows the convergence of the total energy with respect to  $d$ . For  $d < 5.0$  Å, strong interactions between adjacent periodic replicas occur and the relative total energy rises considerably as  $d$  decreases. The total energy obtained for the largest unit cell (with  $d = 30.0$  Å) was employed as reference here. At moderate distances between 5.0 Å and 8.0 Å, the interactions between the periodic images become weaker and the relative total energy approaches convergence with respect to the unit cell size. For  $d > 8.0$  Å, the variations in the relative total energy become smaller than 1 kJ/mol, *i.e.* the total energy reaches independence from  $d$ .

The above investigations demonstrate that the unit cell size should be chosen so large that the minimum distance between periodic images of adsorbates on the surface is at least 8.0 Å. The necessary size of the slab model consequently depends on the size of the adsorbate. For the NHC-ligands studied in this work, a slab size of 8 x 8 metal atoms was found to be sufficient. In order to guarantee the comparability of the results, the same slab size was chosen for all adsorbates.

## 1.5 Choice of the Type of Surface Under Study

When studying the adsorption of NHCs on metal surfaces, the question of the most adequate type of surface to investigate arises. A natural choice would be the most stable type of surface for the metal under study, *i.e.* the fcc(111) surface for Cu, Pd and Au,<sup>13,14</sup> because it is likely to be the most abundant type of surface. However, it is known that, on such surfaces, adatoms become available at elevated temperatures<sup>15-17</sup>, and that NHCs can support or facilitate the extraction of adatoms from the bulk metal.<sup>18-20</sup> Therefore,

a careful assessment of the different options is necessary. Surface types that could be considered include an “adatom decorated” fcc(111) surface (*i.e.* several adatoms are added to the clean surface), an “adatom + deficit” surface (where some metal atoms are pulled out of the bulk to become adatoms, leaving a deficit in the surface), and a “clean” fcc(111) surface without faults. Naturally, there are many more surface reconstructions that could be considered, such as the herringbone reconstruction for Au(111). However, testing and comparing all possibilities is computationally out of reach.

In order to make a decision on which type of surface to use in our production calculations, we used the adsorption of IMe on Au(111) as an example and compared the electronic energies of the “clean” fcc(111) surface without defects with the “adatom + deficit” surface. We also tested a structure in which the NHC-bound Au atom and the adsorbed NHC are lifted about 1.0 Å out of the surface plane. However, this geometry optimization converged to the same structure as the one we obtained on the “clean” Au(111) surface and is thus not discussed further (in the converged structures, the NHC-bound Au atom is slightly lifted out of the surface plane, by approx. 0.4 Å). The results are summarized in Tab. S1 and the optimized adsorption geometries are illustrated in Fig. S8.

**Table S1:** Comparison of the relative electronic (total) energies for IMe adsorbed on a “clean” Au(111) surface without faults and the “adatom + deficit” surface. The “clean” surface was used as a reference, *i.e.* the corresponding relative energies are set to zero.

surface type	rel. $E_{\text{slab}}$	rel. $E_{\text{slab+IMe}}$
“clean” Au(111)	0.0 kJ/mol	0.0 kJ/mol
“adatom + deficit”	155 kJ/mol	88 kJ/mol

It can be seen that the “adatom + deficit” surface (without IMe adsorbed) is more than 150 kJ/mol less stable than the perfect Au(111) surface. With IMe as adsorbate, the relative total energies of the converged structures vary by 88 kJ/mol, with the “clean” surface still being more stable. This nicely shows that the presence of the NHC indeed seems to stabilize the “adatom + deficit” structure. However, the reference structure

with the NHC-bound Au atom only being slightly pulled out of the surface plane is still found to be much more stable. This demonstrates that pulling a surface atom out of the bulk to form an adatom is connected to a relatively large energy penalty, which cannot be compensated by the presence of a single IMe molecule alone. We did not consider the “adatom-decorated” fcc(111) surface further, because simply adding adatoms to the “clean” fcc(111) surface to some extent neglects the effort it takes to pull single metal atoms out of the bulk, and we cannot exclude that this neglect might lead to wrong conclusions about the stability of the system. Note that, under experimental conditions, the gap produced by the extraction of a metal atom from the bulk will probably be filled by another metal atom from deeper within the bulk. Moreover, at high NHC coverages and elevated temperatures, the extraction of several top-layer metal atoms might induce a complete surface reconstruction. However, studying such phenomena requires a more flexible setup of the unit cell (*i.e.* more than four metal layers and more than two relaxed metal layers) and is beyond the scope of this work.

Since the aim of this study is to compare different linkers in bidentate NHC ligands, and the calculations are performed at a temperature of 0 K, the “clean” fcc(111) surface is considered most suitable for this purpose, as it is much more stable than the “adatom + deficit” variant, which is likely to become relevant at elevated temperatures.

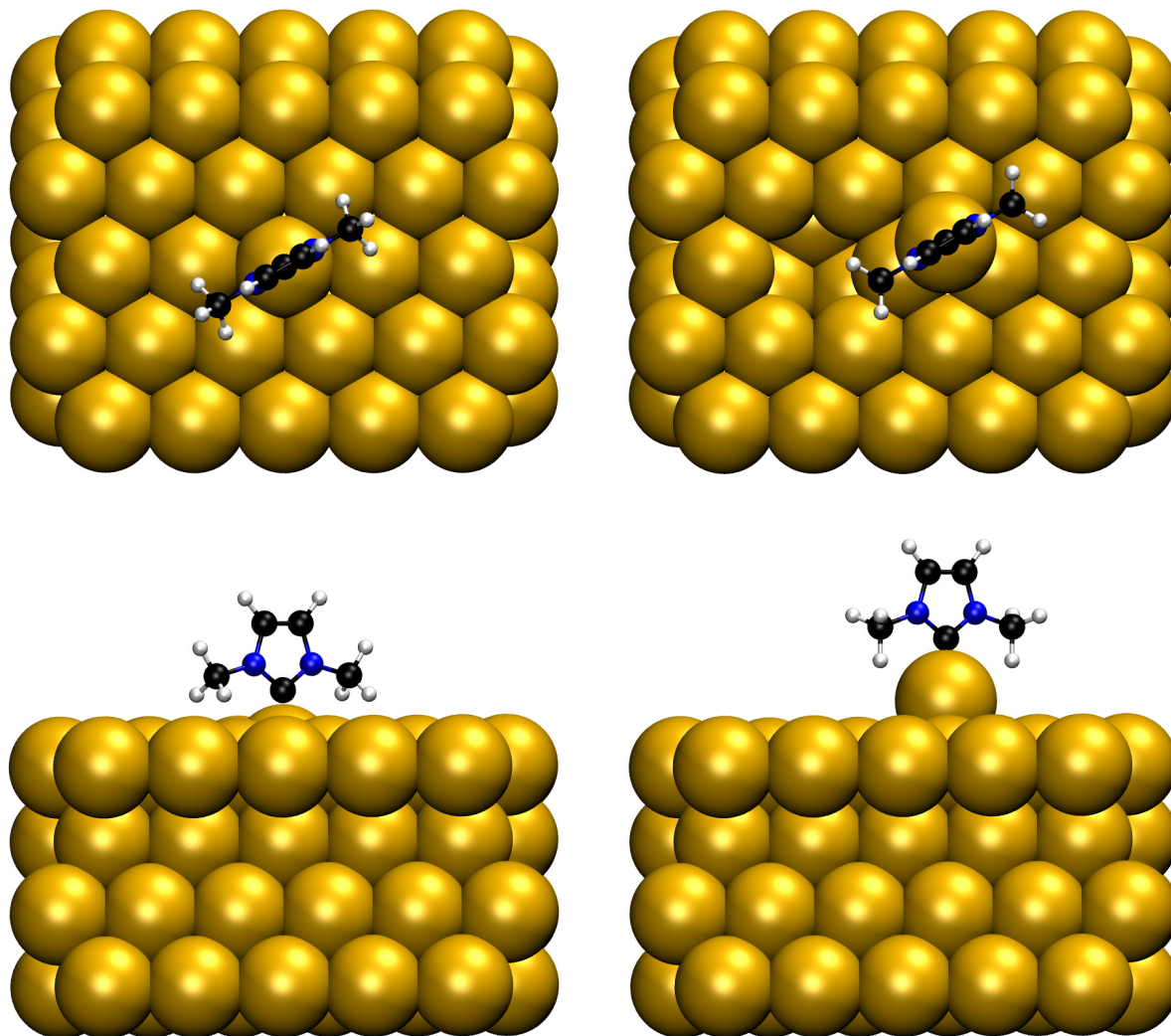


**Figure S8:** Adsorption of IMe on a clean Au(111) surface (left) and on a Au(111) surface, on which the NHC-bound Au atom is extracted from the bulk and acts as an adatom (right). A top view of the structures is shown in the upper row, the lower row shows a side view. Only the relevant sections of the unit cells are illustrated.

## 2 Tilt and Rotation of the NHC Units

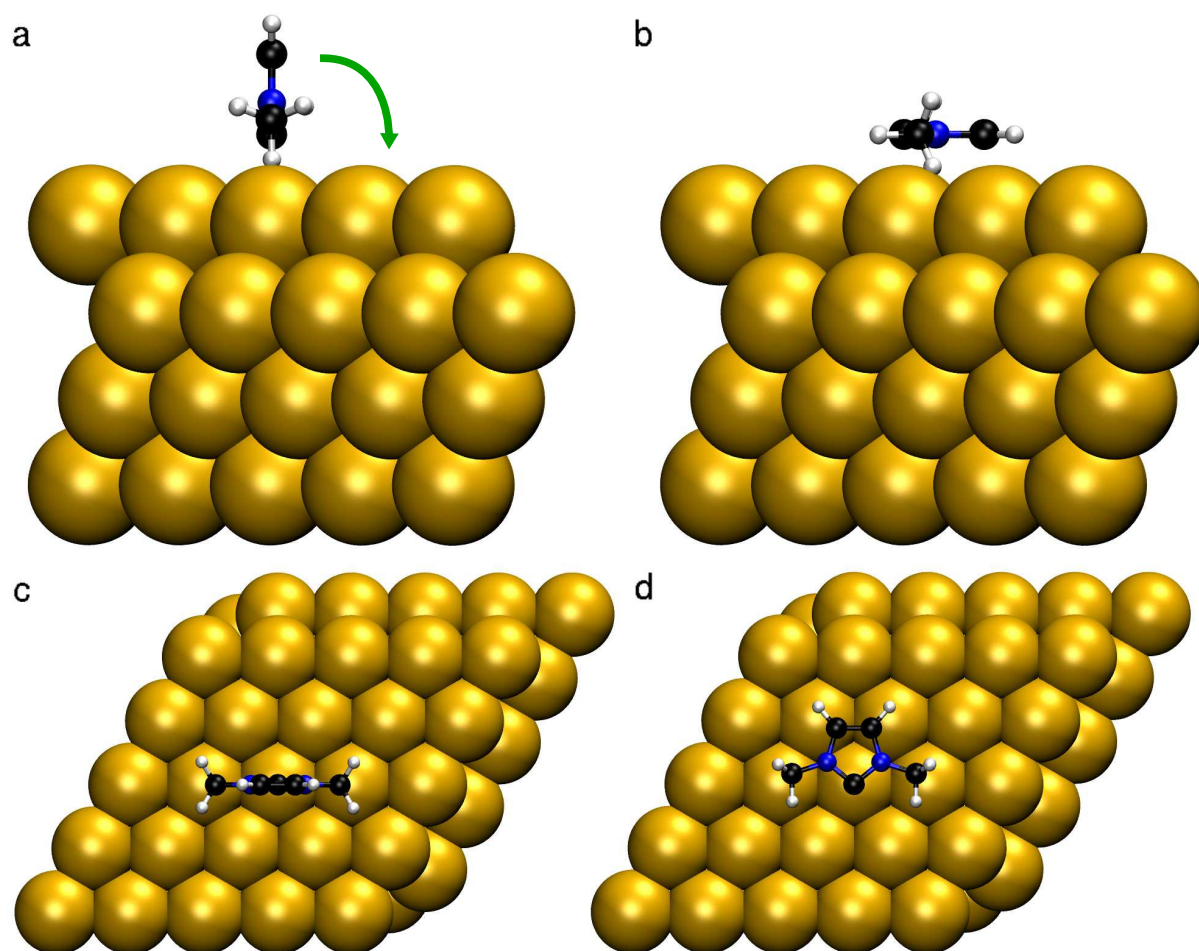


**Figure S9:** Tilt of IMe on the Au(111) surface. The degrees of tilt are shown for an NHC rotated by  $0^\circ$  as an example. **(a)**  $0^\circ$  tilt (side view). The NHC stands upright on the surface. The direction of the tilt is indicated by a green arrow. **(b)**  $90^\circ$  tilt (side view). The NHC lies flat on the surface. **(c)**  $0^\circ$  tilt (top view). **(d)**  $90^\circ$  tilt (top view).

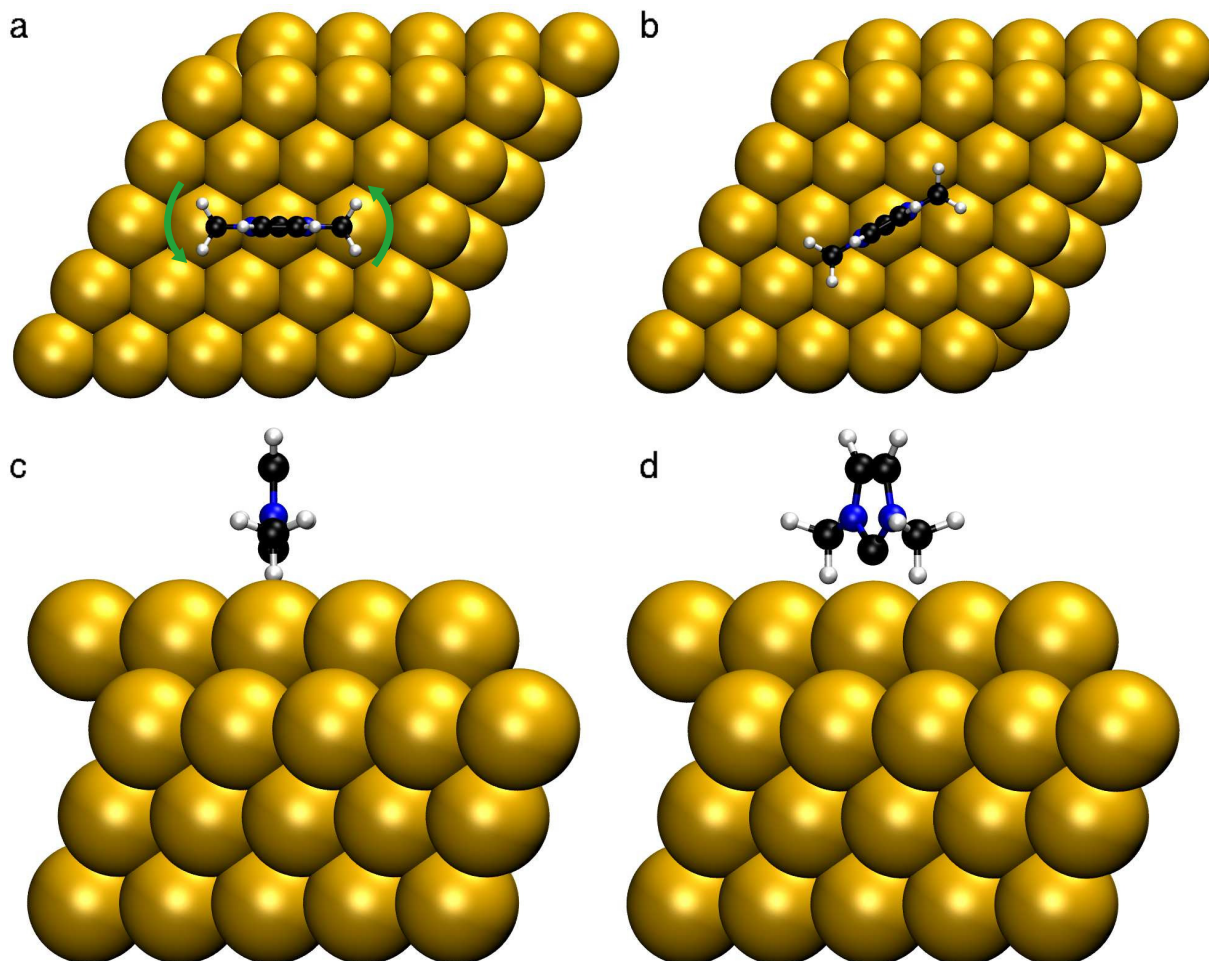


**Figure S10:** Rotation of IMe on the Au(111) surface. The degrees of rotation are shown for an NHC standing upright on the surface as an example. **(a)**  $0^\circ$  rotation (top view). The line connecting the two N atoms is parallel to the row of Au atoms in  $\mathbf{a}_1$ -direction below. The direction of the rotation is indicated by green arrows. **(b)**  $30^\circ$  rotation (top view). The wingtip groups point towards bridge sites between two adjacent Au atoms. **(c)**  $0^\circ$  rotation (side view). **(d)**  $30^\circ$  rotation (side view).

### 3 Investigated Conformers

For most of the bidentate NHC-ligands investigated in our work, several conformers exist and it was impossible to investigate the adsorption properties of all possible structures. However, not all geometries are equally suitable for the adsorption on a metal surface. An important requirement for a tight adsorption of bidentate NHC-ligands is that the carbene carbon atoms of both NHC-units can bind to surface atoms. Structures, in which only one carbene carbon atom points towards the surface result in weak adsorption of the ligands. This is illustrated in Fig. S11. With regard to the increasing complexity of the adsorbates,

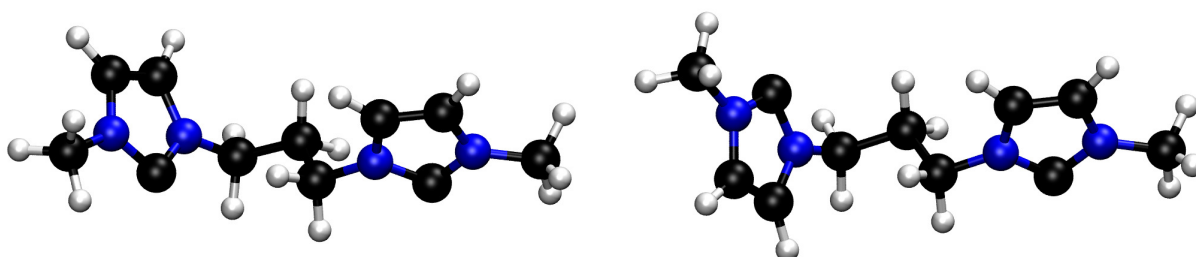


**Figure S11:** Comparison of two converged vacuum structures of **NHC3**. On the left hand side, both carbene carbon atoms point towards similar directions. The geometry is suitable for the adsorption on a metal surface. On the right hand side, the two carbene carbon atoms point in opposite directions. This renders the geometry less suitable for the adsorption on a metal surface.

it is important to keep in mind that geometry optimizations converge to *local* minima in the total energy, and that there is no guarantee that the *global* energy minimum will be found.<sup>21</sup> In practice, this means that starting geometries poorly suited for the adsorption of the bidentate ligands are likely to converge to weakly adsorbing structures, in which only one NHC-unit binds to the surface. In order to save computational resources, the adsorbates were pre-optimized in vacuum (see section on computational details), starting from several structures each. Only well-suited vacuum geometries of the bidentate ligands were subsequently chosen for investigations on the metal surfaces. For **NHC1** to **NHC8**, only one starting geometry was selected. Two different conformers were chosen for **NHC9** (Fig. S12), and three structures were investigated for **NHC10** to **NHC12** (Fig. S13 - S15).

The adsorption geometries of all examined structures are illustrated in Fig. S16 - S34 in the following section. For the main section of this work, the structures which adsorbed strongest on the majority of surfaces (see Tab. S2 - S6) was selected and considered for each ligand. Tab. S4 shows the influence of the NHC unit-adsorption geometry on the adsorption energy of the bidentate ligands, using the conformers of **NHC10** on the Cu(111) surface as an example. It can be seen that the strength of the adsorption decreases with increasing tilt and deviation from an on-top position. The average tilts and average distances of the NHC units from an ideal on-top position of all investigated ligands are listed in Tab. S7 - S9 in the following section.

Note that this work attributes differences in binding energies of bidentate NHCs mainly to the flexibility of the linker (which determines how well the carbenes can adopt the most favorable positions and orientations on the surface), and to direct interactions between the linkers and the surface. Electronic substituent effects of the linker on the carbene seem to have a minor influence on the adsorption energies. This agrees with other studies about NHCs on metal surfaces,<sup>15,22</sup> and seems reasonable, because many substituents arrange in such a way that their interaction with the surface is maximized, *i.e.* they lie as flat on the surface as possible. A plausible explanation why electronic substituent effects play a minor role could be that the carbene-metal bond itself and the van der Waals interactions between the linker and the surface are much stronger than possible electronic substituent effects, so that the latter become hard to detect and have a comparatively small influence. Making comparisons between linkers with larger differences in electronic properties (such as fluorinated linkers vs. unmodified aliphatic/aromatic linkers, for example) could be a possibility to reveal the influence of such effects. This, however, was not considered in the present work.

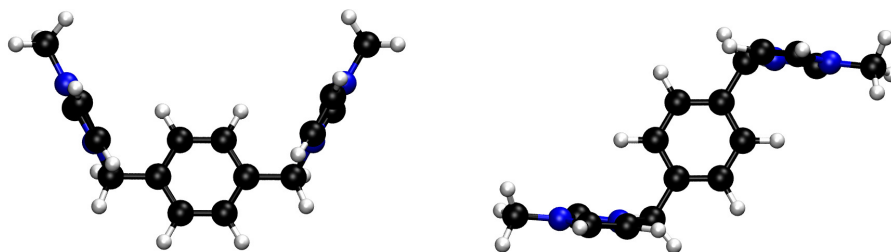


**Figure S12:** Examined structures for **NHC9**. The conformers **NHC9** (left), **NHC9b** (right) have different adsorption properties.

**Table S2:** Adsorption energies of the different conformers of **NHC9** on the three investigated metal surfaces.

	<b>Cu(111)</b>	<b>Pd(111)</b>	<b>Au(111)</b>
<b>NHC9</b>	-437.23 kJ/mol	-651.10 kJ/mol	-417.64 kJ/mol
<b>NHC9b</b>	-441.92 kJ/mol	-648.75 kJ/mol	-405.84 kJ/mol

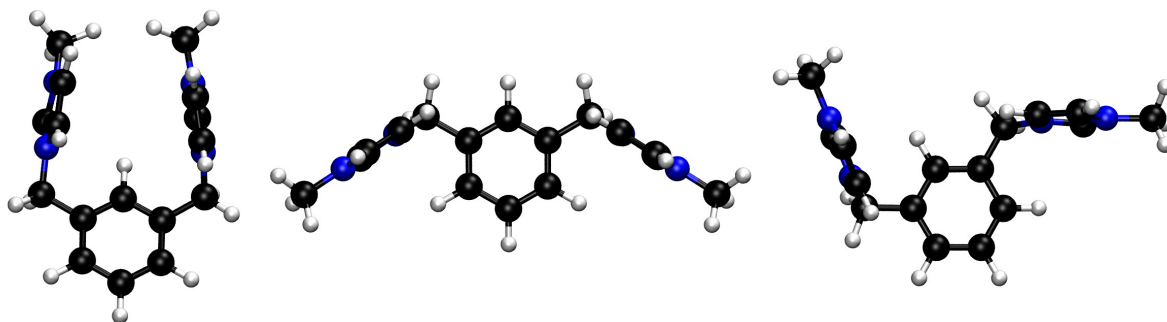


**Figure S13:** Examined structures for **NHC10**. The conformers **NHC10** (left), **NHC10b** (middle) and **NHC10c** (right) have different adsorption properties.

**Table S3:** Adsorption energies of the different conformers of **NHC10** on the three investigated metal surfaces.

	<b>Cu(111)</b>	<b>Pd(111)</b>	<b>Au(111)</b>
<b>NHC10</b>	-435.60 kJ/mol	-671.92 kJ/mol	-409.08 kJ/mol
<b>NHC10b</b>	-403.94 kJ/mol	-637.94 kJ/mol	-401.31 kJ/mol
<b>NHC10c</b>	-421.89 kJ/mol	-647.27 kJ/mol	-414.10 kJ/mol

**Table S4:** Comparison of the adsorption energies, the average tilt and the average horizontal displacement of the NHC units from an ideal on-top position in the three examined conformers of **NHC10** on the Cu(111) surface.

ligand	substrate	$E_{\text{ads.}}$	av. tilt	av. disp. on-top
<b>NHC10</b>	Cu(111)	-435.60 kJ/mol	6.09°	0.18 Å
<b>NHC10b</b>	Cu(111)	-403.94 kJ/mol	14.09°	0.56 Å
<b>NHC10c</b>	Cu(111)	-421.89 kJ/mol	11.79°	0.38 Å

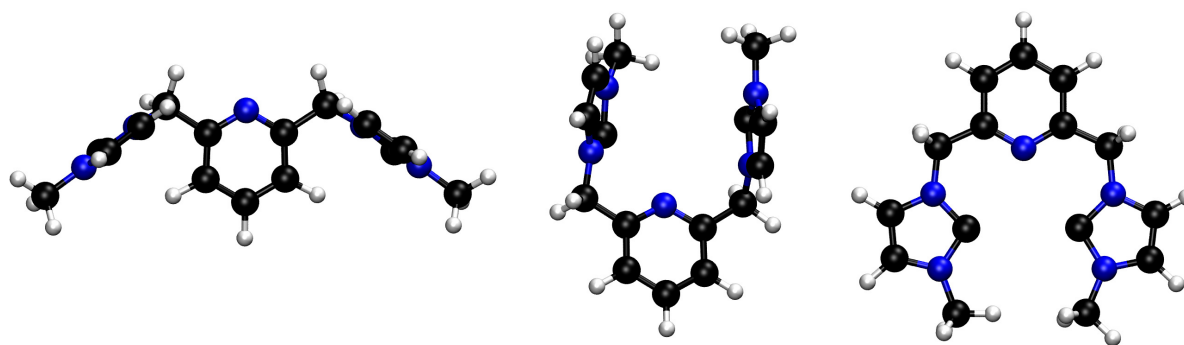


**Figure S14:** Examined structures for **NHC11**. The conformers **NHC11** (left), **NHC11b** (middle) and **NHC11c** (right) have different adsorption properties. Note that the geometry for **NHC11c** was not pre-optimized in vacuum before it was placed on the metal surfaces. This structure was solely used to test whether this ligand is able to form chelating adatom complexes.

**Table S5:** Adsorption energies of the different conformers of **NHC11** on the three investigated metal surfaces.

	<b>Cu(111)</b>	<b>Pd(111)</b>	<b>Au(111)</b>
<b>NHC11</b>	-428.68 kJ/mol	-655.37 kJ/mol	-408.54 kJ/mol
<b>NHC11b</b>	-427.26 kJ/mol	-616.92 kJ/mol	-397.07 kJ/mol
<b>NHC11c</b>	-322.29 kJ/mol	-588.90 kJ/mol	-354.07 kJ/mol

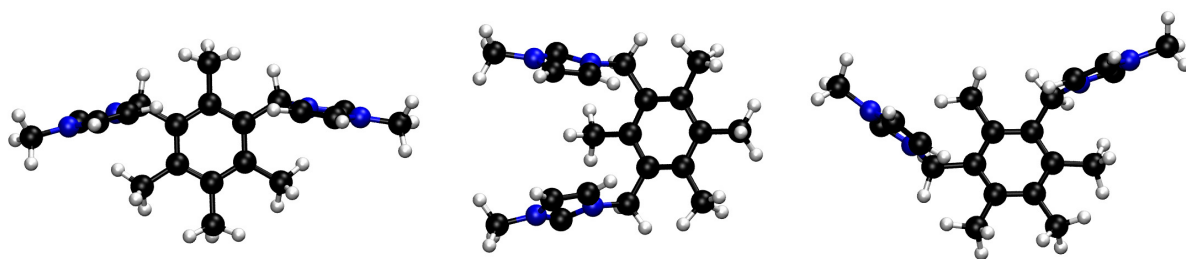


**Figure S15:** Examined structures for **NHC12**. The conformers **NHC12** (left), **NHC12b** (middle) and **NHC12c** (right) have different adsorption properties.

**Table S6:** Adsorption energies of the different conformers of **NHC12** on the three investigated metal surfaces.

	<b>Cu(111)</b>	<b>Pd(111)</b>	<b>Au(111)</b>
<b>NHC12</b>	-427.72 kJ/mol	-609.25 kJ/mol	-413.28 kJ/mol
<b>NHC12b</b>	-435.57 kJ/mol	-586.92 kJ/mol	-392.77 kJ/mol
<b>NHC12c</b>	-432.68 kJ/mol	-588.32 kJ/mol	-408.21 kJ/mol

## 4 Adsorption Geometries of All Investigated Ligands

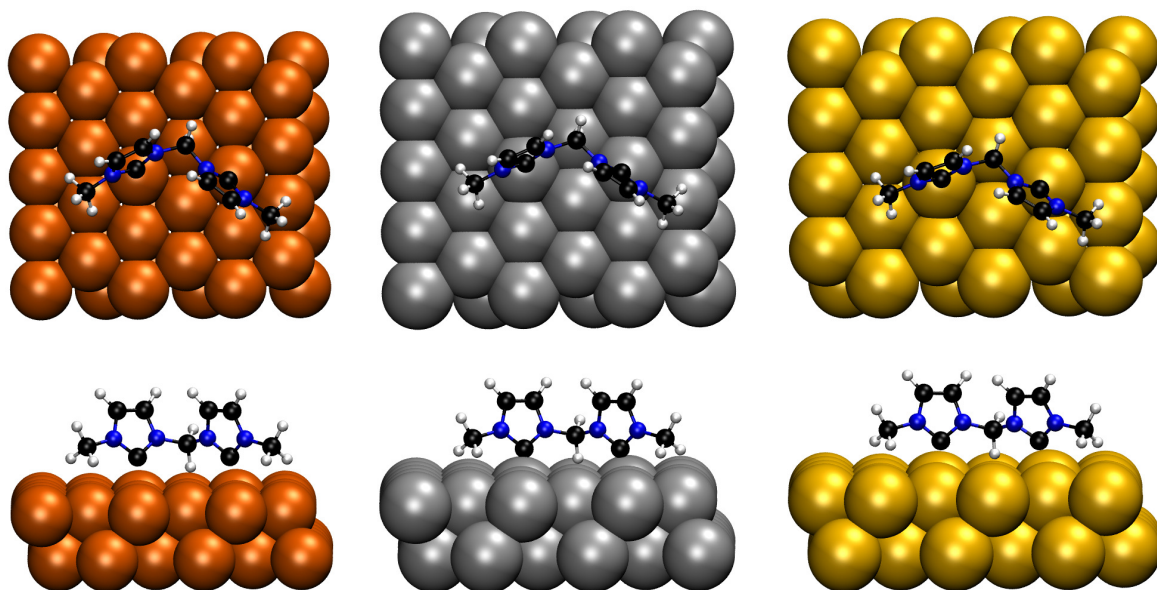


**Figure S16:** Adsorption geometries of NHC1 on the Cu111 (left), Pd(111) (middle) and Au(111) (right) surfaces. A top view of the structures is shown in the upper row, the lower row shows a side perspective. Only the relevant sections of the unit cells are illustrated.

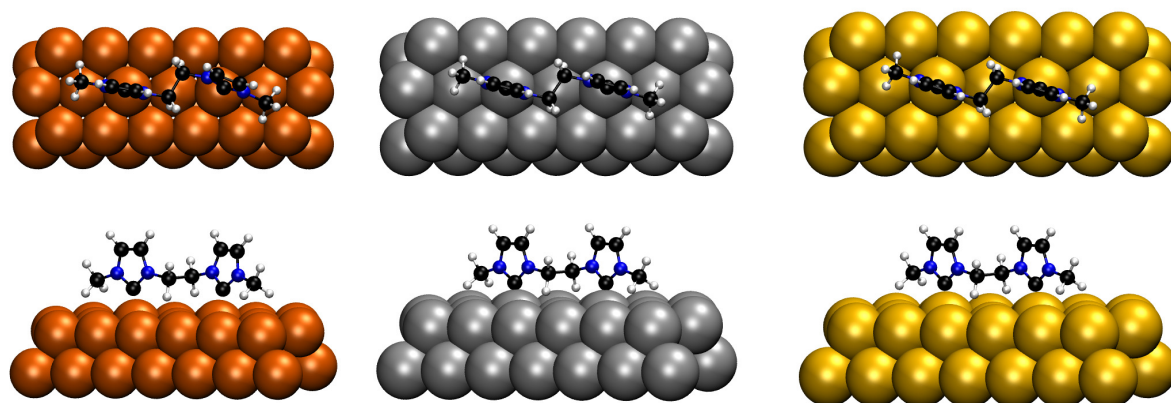


**Figure S17:** Adsorption geometries of NHC2 on the Cu111 (left), Pd(111) (middle) and Au(111) (right) surfaces. A top view of the structures is shown in the upper row, the lower row shows a side perspective. Only the relevant sections of the unit cells are illustrated.

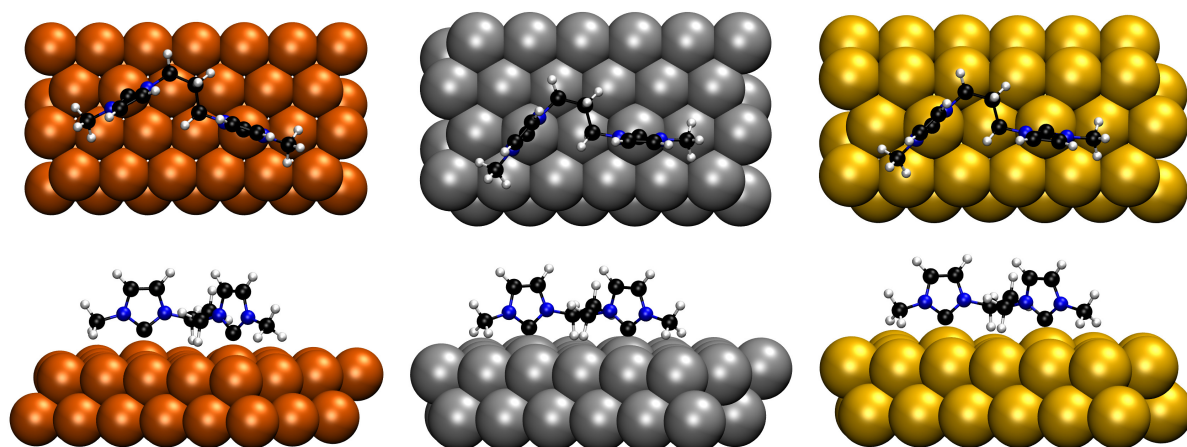


**Figure S18:** Adsorption geometries of **NHC3** on the Cu111 (left), Pd(111) (middle) and Au(111) (right) surfaces. A top view of the structures is shown in the upper row, the lower row shows a side perspective. Only the relevant sections of the unit cells are illustrated.

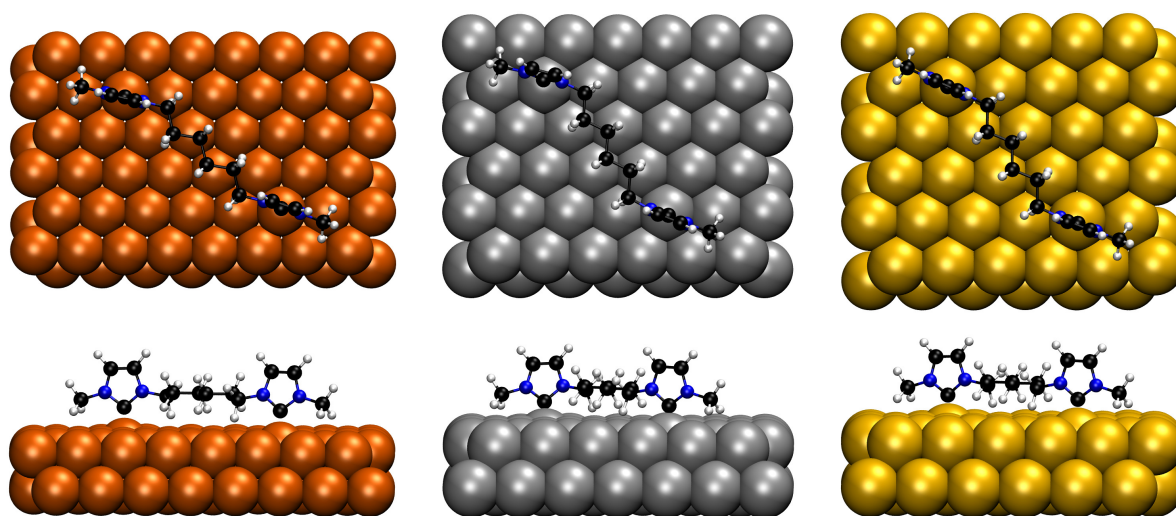


**Figure S19:** Adsorption geometries of **NHC4** on the Cu111 (left), Pd(111) (middle) and Au(111) (right) surfaces. A top view of the structures is shown in the upper row, the lower row shows a side perspective. Only the relevant sections of the unit cells are illustrated.

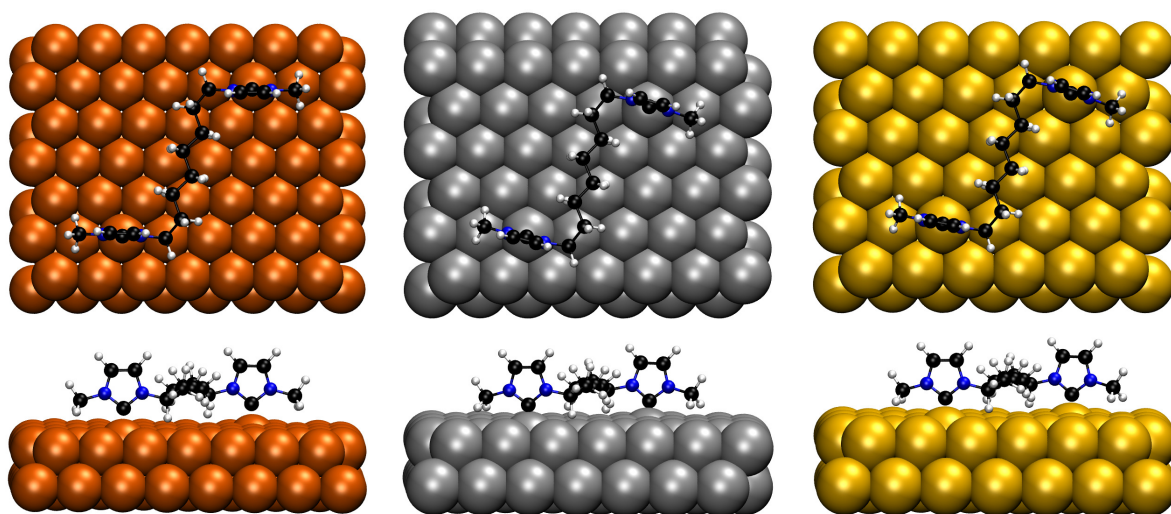


**Figure S20:** Adsorption geometries of **NHC5** on the Cu111 (left), Pd(111) (middle) and Au(111) (right) surfaces. A top view of the structures is shown in the upper row, the lower row shows a side perspective. Only the relevant sections of the unit cells are illustrated.

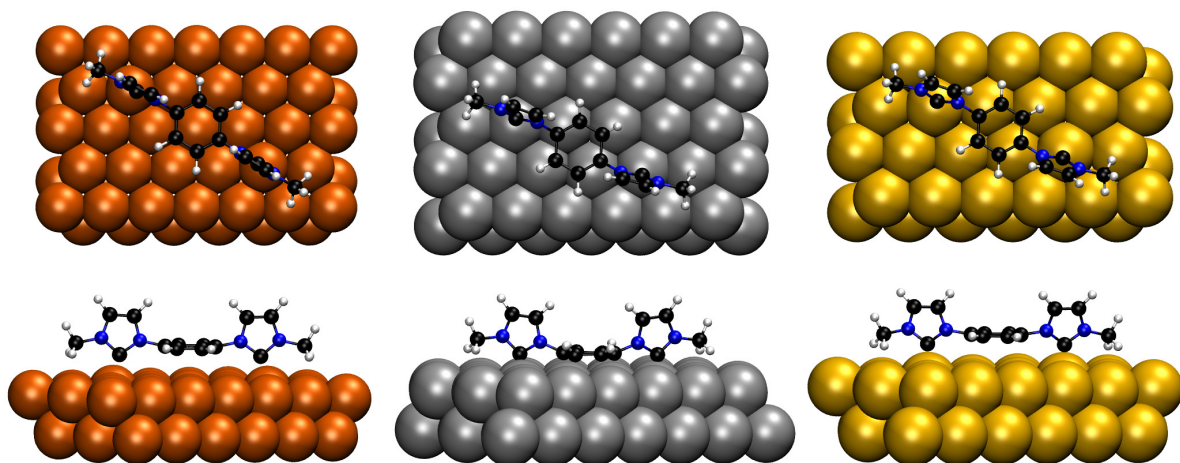


**Figure S21:** Adsorption geometries of **NHC6** on the Cu111 (left), Pd(111) (middle) and Au(111) (right) surfaces. A top view of the structures is shown in the upper row, the lower row shows a side perspective. Only the relevant sections of the unit cells are illustrated.

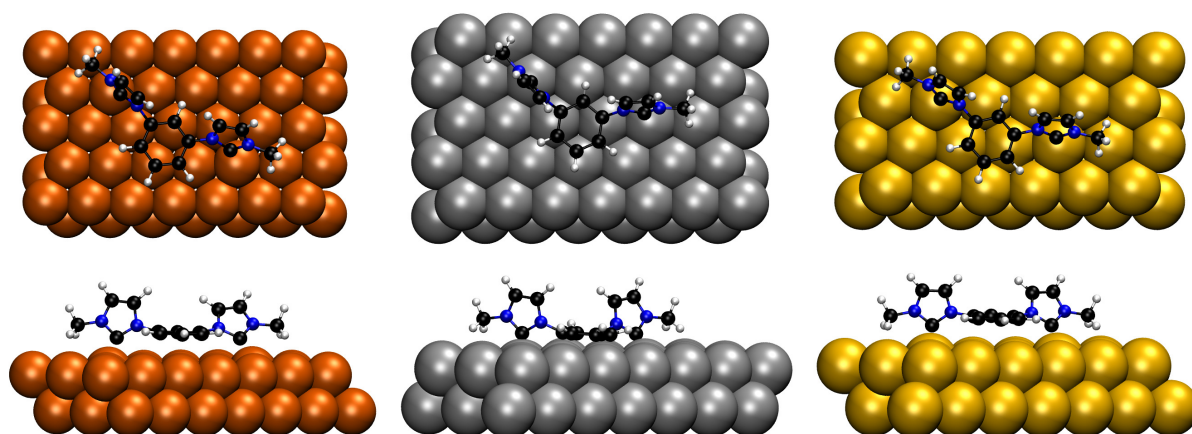


**Figure S22:** Adsorption geometries of NHC7 on the Cu111 (left), Pd(111) (middle) and Au(111) (right) surfaces. A top view of the structures is shown in the upper row, the lower row shows a side perspective. Only the relevant sections of the unit cells are illustrated.

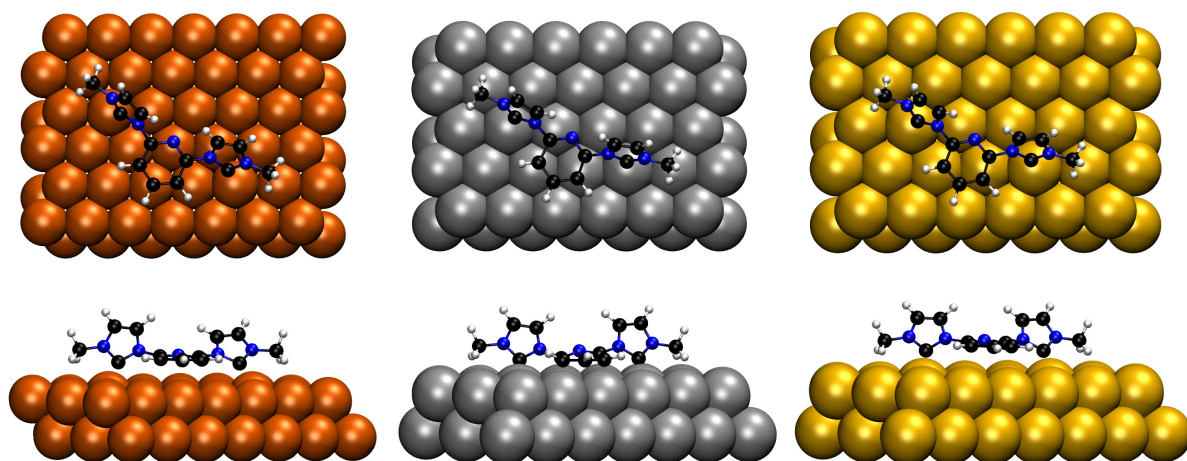


**Figure S23:** Adsorption geometries of NHC8 on the Cu111 (left), Pd(111) (middle) and Au(111) (right) surfaces. A top view of the structures is shown in the upper row, the lower row shows a side perspective. Only the relevant sections of the unit cells are illustrated.

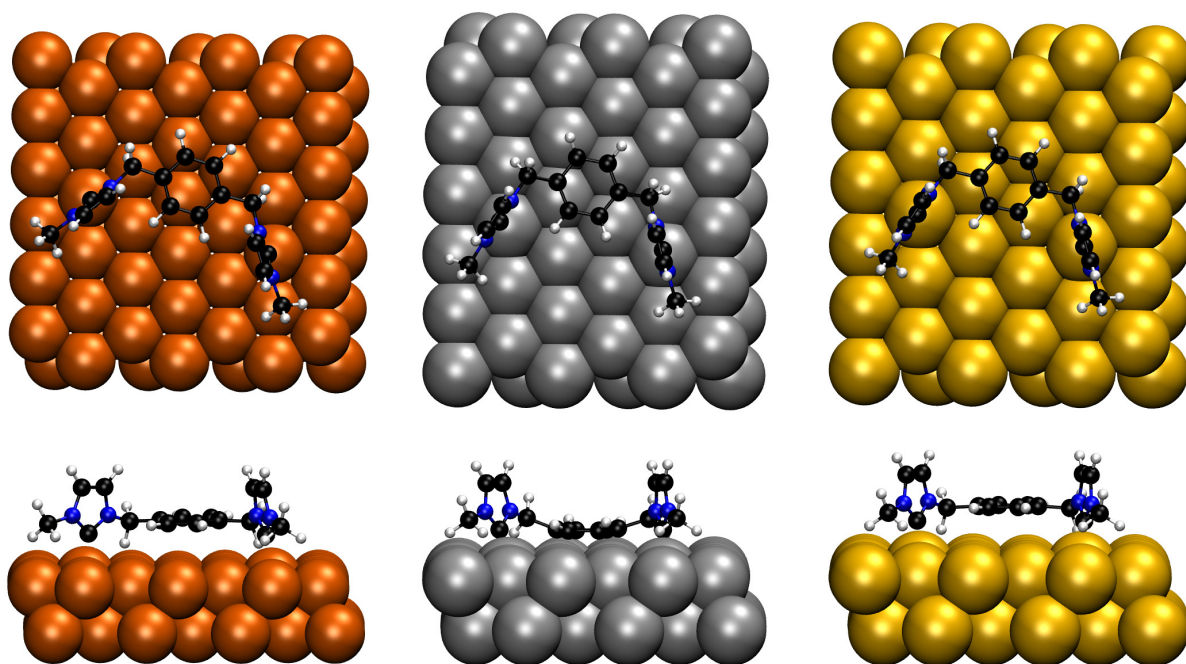


**Figure S24:** Adsorption geometries of NHC9 on the Cu(111) (left), Pd(111) (middle) and Au(111) (right) surfaces. A top view of the structures is shown in the upper row, the lower row shows a side perspective. Only the relevant sections of the unit cells are illustrated.

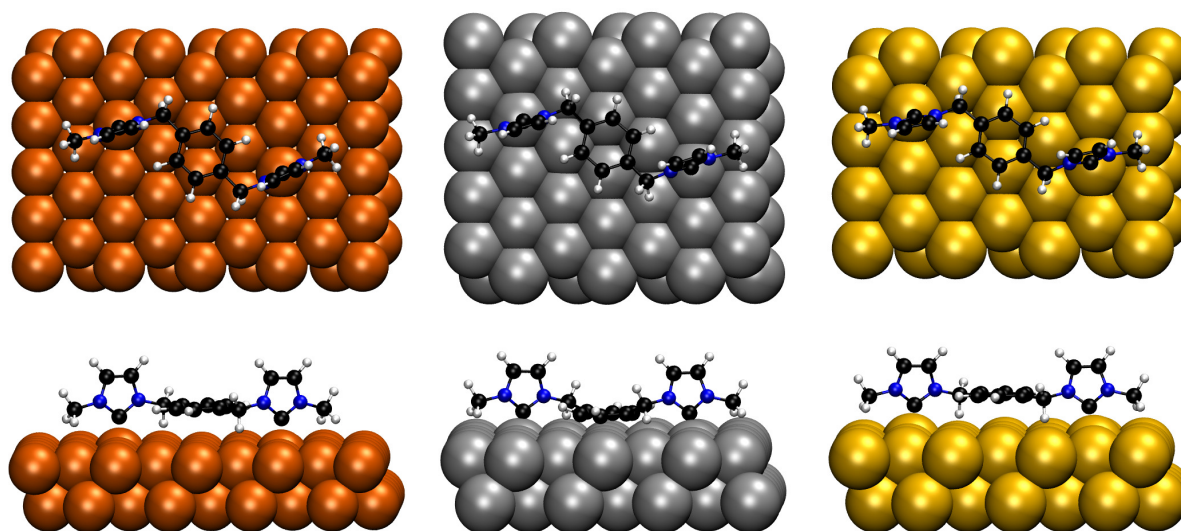


**Figure S25:** Adsorption geometries of NHC9b on the Cu(111) (left), Pd(111) (middle) and Au(111) (right) surfaces. A top view of the structures is shown in the upper row, the lower row shows a side perspective. Only the relevant sections of the unit cells are illustrated.

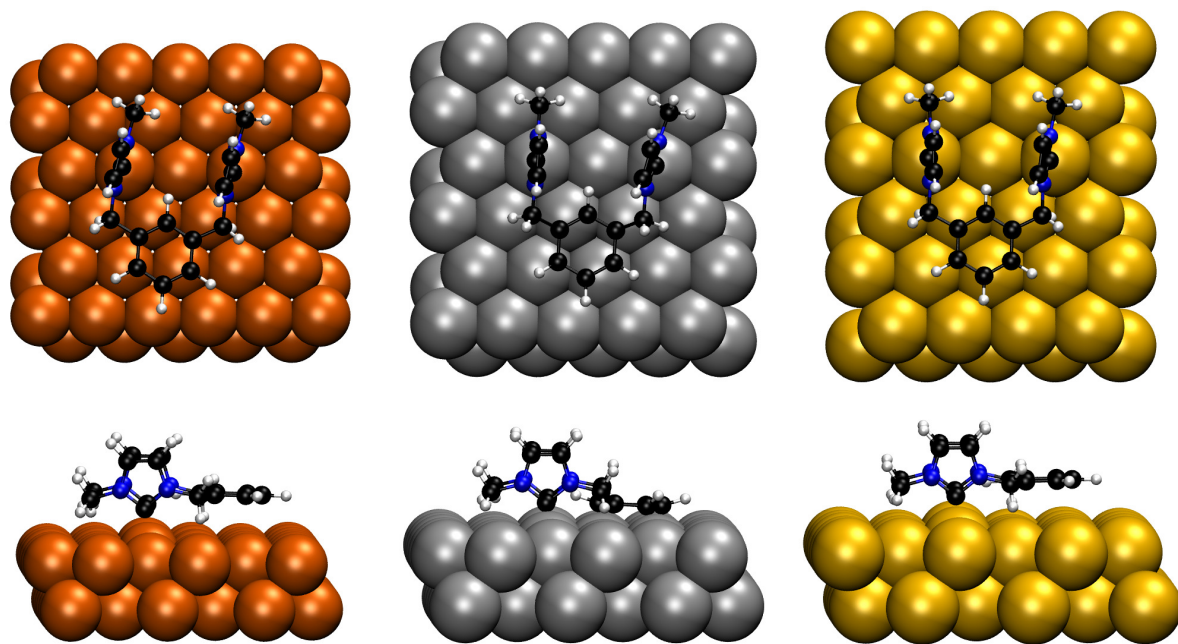


**Figure S26:** Adsorption geometries of **NHC10** on the Cu111 (left), Pd(111) (middle) and Au(111) (right) surfaces. A top view of the structures is shown in the upper row, the lower row shows a side perspective. Only the relevant sections of the unit cells are illustrated.

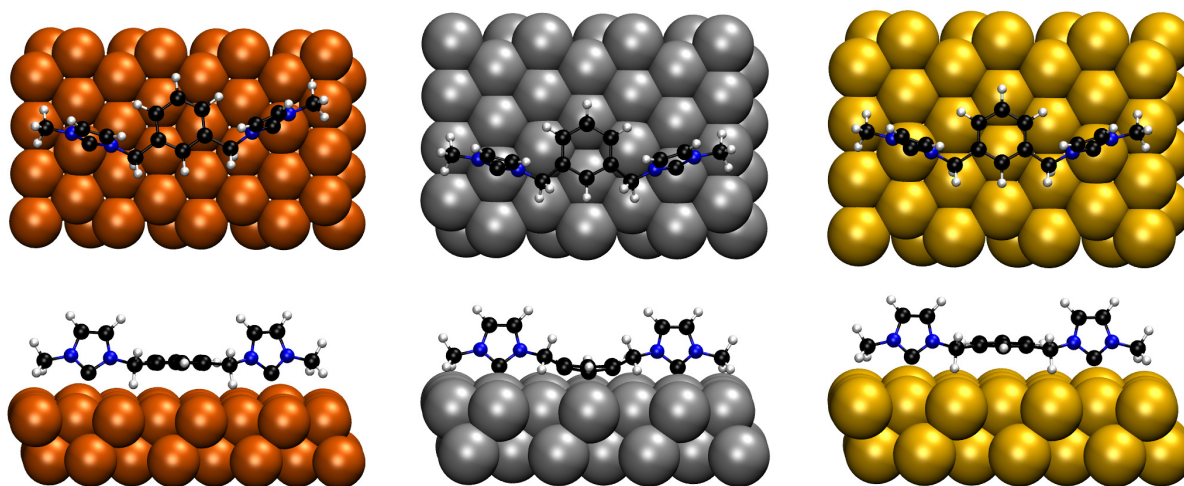


**Figure S27:** Adsorption geometries of **NHC10b** on the Cu111 (left), Pd(111) (middle) and Au(111) (right) surfaces. A top view of the structures is shown in the upper row, the lower row shows a side perspective. Only the relevant sections of the unit cells are illustrated.

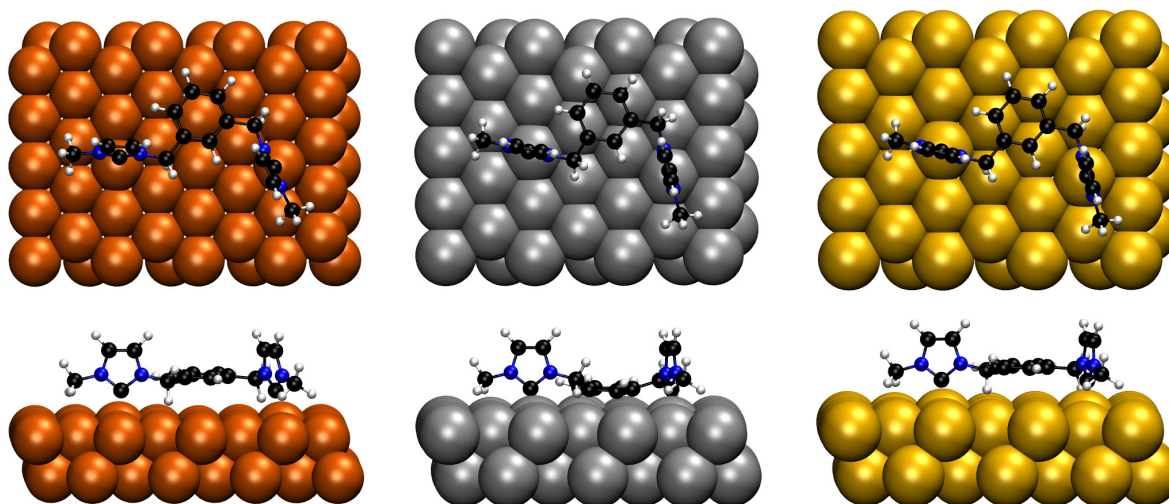


**Figure S28:** Adsorption geometries of NHC10c on the Cu111 (left), Pd(111) (middle) and Au(111) (right) surfaces. A top view of the structures is shown in the upper row, the lower row shows a side perspective. Only the relevant sections of the unit cells are illustrated.

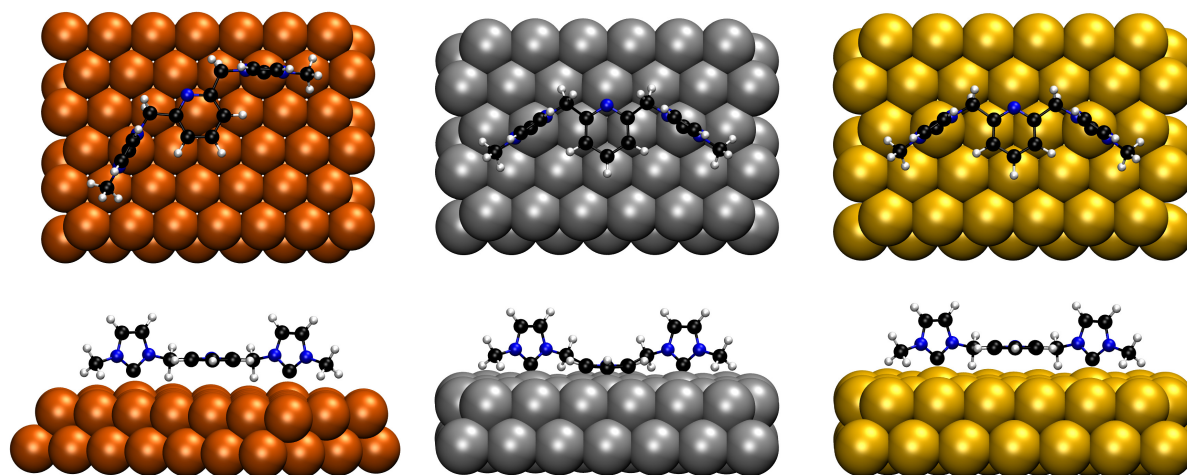


**Figure S29:** Adsorption geometries of NHC11 on the Cu111 (left), Pd(111) (middle) and Au(111) (right) surfaces. A top view of the structures is shown in the upper row, the lower row shows a side perspective. Only the relevant sections of the unit cells are illustrated.

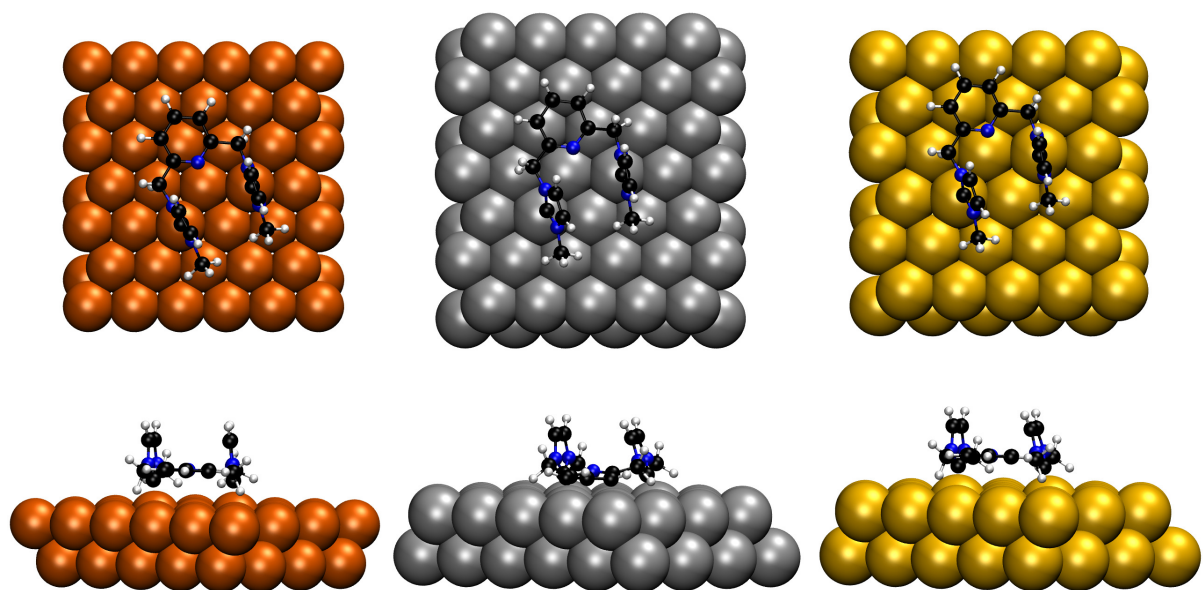


**Figure S30:** Adsorption geometries of **NHC11b** on the Cu111 (left), Pd(111) (middle) and Au(111) (right) surfaces. A top view of the structures is shown in the upper row, the lower row shows a side perspective. Only the relevant sections of the unit cells are illustrated.

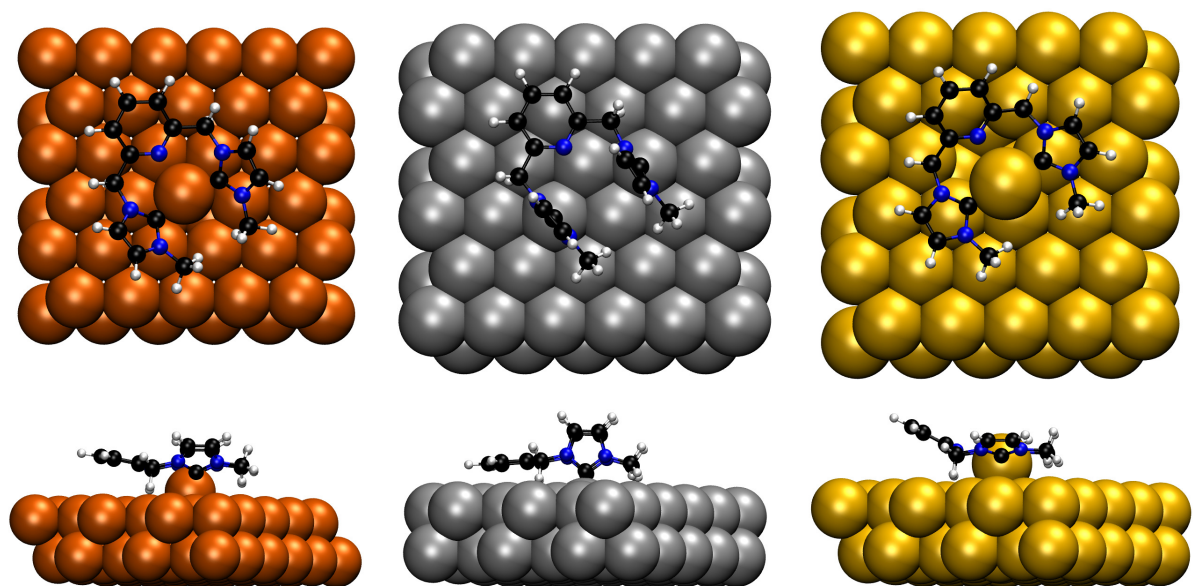


**Figure S31:** Adsorption geometries of **NHC11c** on the Cu111 (left), Pd(111) (middle) and Au(111) (right) surfaces. A top view of the structures is shown in the upper row, the lower row shows a side perspective. Only the relevant sections of the unit cells are illustrated.

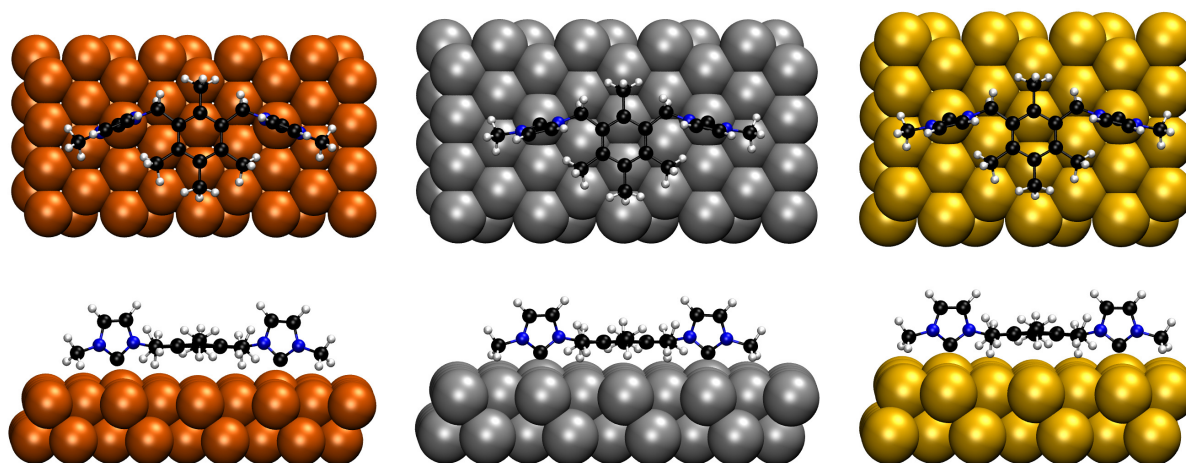


**Figure S32:** Adsorption geometries of **NHC12** on the Cu111 (left), Pd(111) (middle) and Au(111) (right) surfaces. A top view of the structures is shown in the upper row, the lower row shows a side perspective. Only the relevant sections of the unit cells are illustrated.

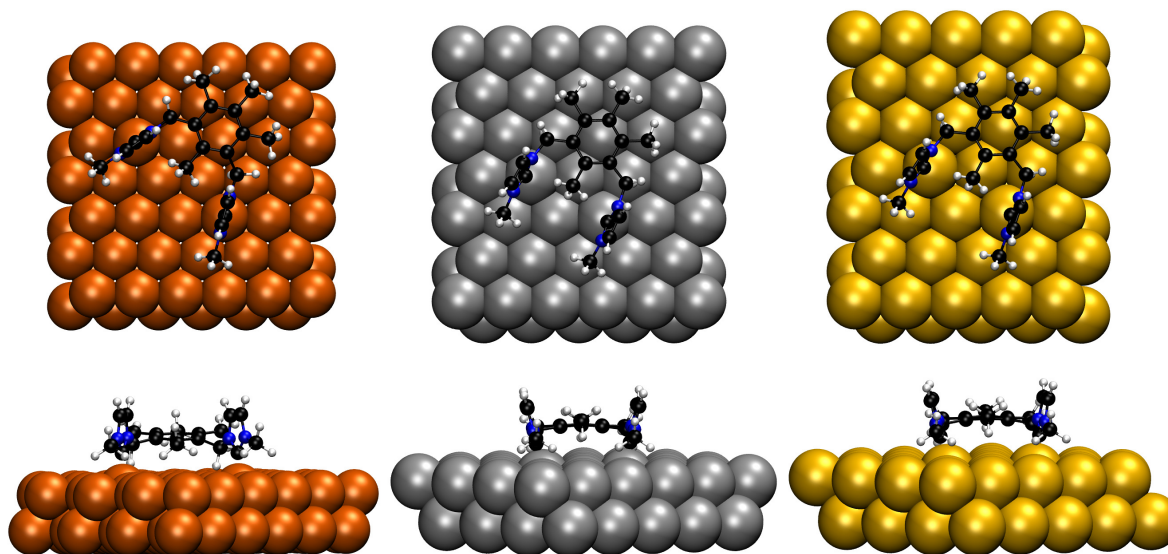


**Figure S33:** Adsorption geometries of **NHC12b** on the Cu111 (left), Pd(111) (middle) and Au(111) (right) surfaces. A top view of the structures is shown in the upper row, the lower row shows a side perspective. Only the relevant sections of the unit cells are illustrated.

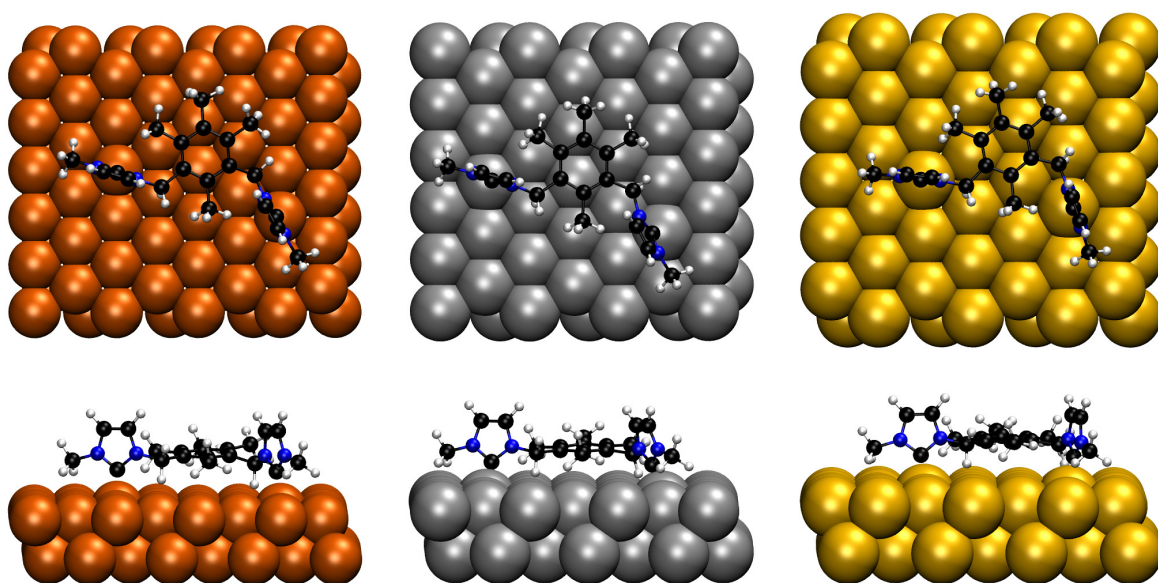


**Figure S34:** Adsorption geometries of **NHC12c** on the Cu(111) (left), Pd(111) (middle) and Au(111) (right) surfaces. A top view of the structures is shown in the upper row, the lower row shows a side perspective. Only the relevant sections of the unit cells are illustrated.

**Table S7:** Comparison of the average tilt, the average horizontal displacement of the NHC units from an ideal on-top position and the average out-of-plane ( $z$ -direction) movement of the two NHC-bound metal atoms in all examined bidentate ligands on the Cu(111) surface.

ligand	substrate	av. tilt	av. disp. on-top	av. $z$ -movement
NHC1	Cu(111)	16.60°	0.33 Å	0.32 Å
NHC2	Cu(111)	7.26°	0.25 Å	0.38 Å
NHC3	Cu(111)	5.48°	0.24 Å	0.39 Å
NHC4	Cu(111)	3.95°	0.12 Å	0.39 Å
NHC5	Cu(111)	4.17°	0.15 Å	0.39 Å
NHC6	Cu(111)	3.21°	0.35 Å	0.31 Å
NHC7	Cu(111)	23.73°	0.70 Å	0.31 Å
NHC8	Cu(111)	30.62°	0.78 Å	0.35 Å
NHC9	Cu(111)	8.77°	0.24 Å	0.38 Å
NHC9b	Cu(111)	3.97°	0.11 Å	0.38 Å
NHC10	Cu(111)	6.09°	0.18 Å	0.38 Å
NHC10b	Cu(111)	14.09°	0.56 Å	0.41 Å
NHC10c	Cu(111)	11.79°	0.38 Å	0.41 Å
NHC11	Cu(111)	3.31°	0.13 Å	0.37 Å
NHC11b	Cu(111)	4.40°	0.13 Å	0.38 Å
NHC11c	Cu(111)	49.46°	1.73 Å	1.65 Å
NHC12	Cu(111)	0.52°	0.26 Å	0.40 Å
NHC12b	Cu(111)	1.89°	0.09 Å	0.40 Å
NHC12c	Cu(111)	4.58°	0.18 Å	0.40 Å

**Table S8:** Comparison of the average tilt, the average horizontal displacement of the NHC units from an ideal on-top position and the average out-of-plane ( $z$ -direction) movement of the two NHC-bound metal atoms in all examined bidentate ligands on the Pd(111) surface.

ligand	substrate	av. tilt	av. disp. on-top	av. $z$ -movement
NHC1	Pd(111)	11.53°	0.31 Å	0.27 Å
NHC2	Pd(111)	2.80°	0.12 Å	0.31 Å
NHC3	Pd(111)	5.12°	0.18 Å	0.34 Å
NHC4	Pd(111)	7.55°	0.23 Å	0.34 Å
NHC5	Pd(111)	6.54°	0.17 Å	0.32 Å
NHC6	Pd(111)	13.08°	0.34 Å	0.12 Å
NHC7	Pd(111)	11.55°	0.36 Å	0.14 Å
NHC8	Pd(111)	22.62°	0.62 Å	0.21 Å
NHC9	Pd(111)	4.75°	0.32 Å	0.26 Å
NHC9b	Pd(111)	8.98°	0.24 Å	0.26 Å
NHC10	Pd(111)	5.80°	0.15 Å	0.26 Å
NHC10b	Pd(111)	14.49°	0.37 Å	0.27 Å
NHC10c	Pd(111)	2.19°	0.26 Å	0.25 Å
NHC11	Pd(111)	3.41°	0.21 Å	0.23 Å
NHC11b	Pd(111)	12.44°	0.39 Å	0.27 Å
NHC11c	Pd(111)	5.81°	0.16 Å	0.31 Å
NHC12	Pd(111)	8.98°	0.24 Å	0.33 Å
NHC12b	Pd(111)	11.65°	0.32 Å	0.32 Å
NHC12c	Pd(111)	10.84°	0.41 Å	0.36 Å

**Table S9:** Comparison of the average tilt, the average horizontal displacement of the NHC units from an ideal on-top position and the average out-of-plane ( $z$ -direction) movement of the two NHC-bound metal atoms in all examined bidentate ligands on the Au(111) surface.

ligand	substrate	av. tilt	av. disp. on-top	av. $z$ -movement
NHC1	Au(111)	17.03°	0.38 Å	0.33 Å
NHC2	Au(111)	1.51°	0.08 Å	0.36 Å
NHC3	Au(111)	7.89°	0.18 Å	0.39 Å
NHC4	Au(111)	1.96°	0.08 Å	0.39 Å
NHC5	Au(111)	3.49°	0.08 Å	0.40 Å
NHC6	Au(111)	20.51°	0.36 Å	0.31 Å
NHC7	Au(111)	23.92°	0.41 Å	0.33 Å
NHC8	Au(111)	30.96°	0.49 Å	0.36 Å
NHC9	Au(111)	3.40°	0.11 Å	0.37 Å
NHC9b	Au(111)	13.08°	0.32 Å	0.40 Å
NHC10	Au(111)	7.77°	0.20 Å	0.39 Å
NHC10b	Au(111)	11.92°	0.29 Å	0.40 Å
NHC10c	Au(111)	2.74°	0.11 Å	0.37 Å
NHC11	Au(111)	4.80°	0.14 Å	0.37 Å
NHC11b	Au(111)	8.97°	0.21 Å	0.39 Å
NHC11c	Au(111)	66.54°	2.00 Å	2.59 Å
NHC12	Au(111)	7.71°	0.18 Å	0.43 Å
NHC12b	Au(111)	10.96°	0.32 Å	0.41 Å
NHC12c	Au(111)	4.00°	0.22 Å	0.40 Å

## 5 Acknowledgements

The authors gratefully acknowledge the financial support by the Deutsche Forschungsgemeinschaft (DFG) within the collaborative research center SFB 858 (project Z01). Moreover, we thank Dr. Dennis Barton, Dr. Christian Mück-Lichtenfeld, Prof. Dr. Frank Glorius and Matthias Freitag for fruitful discussions and helpful advice.

## 6 References

- [1] J. Perdew, K. Burke and M. Ernzerhof, *Phys. Rev. Lett.*, 1996, **77**, 3865–3868.
- [2] J. Perdew, K. Burke and M. Ernzerhof, *Phys. Rev. Lett.*, 1997, **78**, 1396.
- [3] S. Grimme, J. Antony, S. Ehrlich and H. Krieg, *J. Chem. Phys.*, 2010, **132**, 154104.
- [4] S. Grimme, S. Ehrlich and L. Goerigk, *J. Comput. Chem.*, 2011, **32**, 1456–1465.
- [5] A. D. Becke and E. R. Johnson, *J. Chem. Phys.*, 2005, **123**, 154101.
- [6] E. R. Johnson and A. D. Becke, *J. Chem. Phys.*, 2005, **123**, 024101.
- [7] E. R. Johnson and A. D. Becke, *J. Chem. Phys.*, 2006, **124**, 174104.
- [8] M. Dion, H. Rydberg, E. Schröder, D. C. Langreth and B. I. Lundqvist, *Phys. Rev. Lett.*, 2004, **92**, 246401.
- [9] J. Klimeš, D. R. Bowler and A. Michaelides, *J. Phys. Condens. Matter*, 2009, **22**, 022201.
- [10] R. Dronskowski and R. Hoffmann, in *Computational Chemistry of Solid State Materials: A Guide for Materials Scientists, Chemists, Physicists and others*, Wiley, 2006, ch. 2, pp. 45–164.

- [11] H. J. Monkhorst and J. D. Pack, *Phys. Rev. B*, 1976, **13**, 5188–5192.
- [12] D. S. Scholl and J. A. Steckel, in *Density Functional Theory: A Practical Introduction*, John Wiley & Sons, 2009, ch. 3, pp. 49–82.
- [13] E.-C. Fritz, C. Nimphius, A. Goez, S. Würtz, M. Peterlechner, J. Neugebauer, F. Glorius and B. J. Ravoo, *Chem. Eur. J.*, 2015, **21**, 4541–4545.
- [14] M. Rodriguez-Castillo, D. Laurencin, F. Tielens, A. van der Lee, S. Clement, Y. Guari and S. Richeter, *Dalton Trans.*, 2014, **43**, 5978–5982.
- [15] Q. Tang and D.-e. Jiang, *Chem. Mater.*, 2017, **29**, 6908–6915.
- [16] P. Maksymovych, O. Voznyy, D. B. Dougherty, D. C. Sorescu and J. T. Yates, *Prog. Surf. Sci.*, 2010, **85**, 206–240.
- [17] D. Barton, H.-Y. Gao, P. A. Held, A. Studer, H. Fuchs, N. L. Doltsinis and J. Neugebauer, *Chem. Eur. J.*, 2017, **23**, 6190–6197.
- [18] G. Wang, A. Rühling, S. Amirjalayer, M. Knor, J. B. Ernst, C. Richter, H.-J. Gao, A. Timmer, H.-Y. Gao, N. L. Doltsinis, F. Glorius and H. Fuchs, *Nat. Chem.*, 2017, **9**, 152–156.
- [19] C. R. Larrea, C. J. Baddeley, M. R. Narouz, N. J. Mosey, J. H. Horton and C. M. Crudden, *ChemPhysChem*, 2017, **18**, 3536–3539.
- [20] A. Bakker, A. Timmer, E. Kolodzeiski, M. Freitag, H. Y. Gao, H. Mönig, S. Amirjalayer, F. Glorius and H. Fuchs, *J. Am. Chem. Soc.*, 2018, **140**, 11889–11892.
- [21] D. S. Scholl and J. A. Steckel, in *Density Functional Theory: A Practical Introduction*, John Wiley & Sons, 2009, ch. 10, pp. 109–234.
- [22] H. K. Kim, A. S. Hyla, P. Winget, H. Li, C. M. Wyss, A. J. Jordan, F. A. Larrain, J. P. Sadighi, C. Fuentes-Hernandez, B. Kippelen, J.-L. Brédas, S. Barlow and S. R. Marder, *Chem. Mater.*, 2017, **29**, 3403–3411.